



# In-Flight Calibration and Performance of the OSIRIS-REx Touch And Go Camera System (TAGCAMS)

**B.J. Bos<sup>1</sup> · D.S. Nelson<sup>2</sup> · J.Y. Pelgrift<sup>2</sup> · A.J. Liounis<sup>1</sup> · D. Doelling<sup>3</sup> · C.D. Norman<sup>4</sup> · R.D. Olds<sup>4</sup> · C.W. May<sup>4</sup> · R. Witherspoon<sup>4</sup> · E. Church<sup>4</sup> · D. Huish<sup>4</sup> · C.D. Adam<sup>2</sup> · E. Sahr<sup>2</sup> · J. Kidd<sup>5</sup> · K. Drozd<sup>5</sup> · W.M. Owen<sup>6</sup> · M.C. Moreau<sup>1</sup> · L.T. Seals<sup>1</sup> · J. Butt<sup>1</sup> · D. LeDuc<sup>1</sup> · K. Alkiek<sup>1</sup> · L.R. Chevres-Fernandez<sup>1</sup> · K.E. Gordon<sup>1</sup> · K. Khlopenkov<sup>7</sup> · C. Haney<sup>7</sup> · R. Bhatt<sup>7</sup> · J. Hikes<sup>1</sup> · A. Wolfram<sup>1</sup> · M. Caplinger<sup>8</sup> · M.A. Ravine<sup>8</sup> · K. Getzandanner<sup>1</sup> · A. Bartels<sup>1</sup> · D.S. Lauretta<sup>5</sup>**

Received: 25 October 2019 / Accepted: 27 April 2020 / Published online: 10 June 2020

© This is a U.S. government work and not under copyright protection in the U.S.; foreign copyright protection may apply 2020

**Abstract** The Touch And Go Camera System (TAGCAMS) is a three-camera-head instrument onboard NASA's OSIRIS-REx asteroid sample return mission spacecraft. The purpose of TAGCAMS is to facilitate navigation to the target asteroid, (101955) Bennu; confirm acquisition of the asteroid sample; document asteroid sample stowage; and provide supplementary imaging for OSIRIS-REx science investigations.

During the almost two-year OSIRIS-REx outbound cruise phase we pursued nine TAGCAMS imaging campaigns to check, calibrate and characterize the camera system's performance before asteroid arrival and proximity operations began in late 2018. The TAGCAMS in-flight calibration dataset provides the relevant information to enable the three cameras to complete their primary observation goals during asteroid operations. The key performance parameters that we investigated in flight included: linearity, responsivity (both point source and extended body), dark current, hot pixels, pointing, image geometry transformation, im-

---

OSIRIS-REx

Edited by Dante Lauretta and Christopher T. Russell

---

✉ B.J. Bos  
[brent.j.bos@nasa.gov](mailto:brent.j.bos@nasa.gov)

<sup>1</sup> NASA Goddard Space Flight Center, Greenbelt, MD, USA

<sup>2</sup> KinetX Inc., Simi Valley, CA, USA

<sup>3</sup> NASA Langley Research Center, Hampton, VA, USA

<sup>4</sup> Lockheed Martin Space, Littleton, CO, USA

<sup>5</sup> Lunar and Planetary Laboratory, University of Arizona, Tucson, AZ, USA

<sup>6</sup> Jet Propulsion Laboratory, Pasadena, CA, USA

<sup>7</sup> Science Systems and Applications, Inc., Hampton, VA, USA

<sup>8</sup> Malin Space Science Systems, San Diego, CA, USA

age quality and stray light. Analyses of the in-flight performance either confirmed the continued applicability of the TAGCAMS ground test results or substantially improved upon the ground test knowledge. In addition, the TAGCAMS calibration observations identified the source of a spacecraft outgassing feature that guided successful remediation efforts prior to asteroid arrival.

**Keywords** Bennu · Cameras · Spacecraft · Remote sensing · Instruments · Imaging systems · Planetary missions · Asteroid · Sample return

## 1 Introduction and Overview

The National Aeronautics and Space Administration (NASA) launched the OSIRIS-REx (Origins, Spectral Interpretation, Resource Identification, and Security-Regolith Explorer) asteroid sample return mission on September 8, 2016. The mission's objective is to travel to the near-Earth asteroid (101955) Bennu, survey and map its surface, obtain at least 60 g of surface material and return the sample to Earth in 2023 (Lauretta et al. 2017).

Among the instruments onboard the OSIRIS-REx spacecraft is the Touch And Go Camera System (TAGCAMS). TAGCAMS is a three-camera-head system with two onboard digital video recorders (DVR) mounted to the spacecraft nadir deck. The three cameras support spacecraft navigation, sample acquisition, sample stowage and provide supplementary imaging for OSIRIS-REx science investigations. All three cameras have a  $2592 \times 1944$  pixel complementary metal oxide semiconductor (CMOS) detector array that provides up to 12-bit pixel depth. The three cameras also share the same lens design and a camera field of view of roughly  $44^\circ \times 32^\circ$  with a pixel scale of 0.28 mrad/pixel.

The TAGCAMS primary navigation camera is called NavCam 1. The back-up navigation camera and primary natural feature tracking (NFT) camera is called NavCam 2. StowCam is used to verify asteroid sample stowage in the spacecraft's sample return capsule (SRC). NavCam 1 and 2 are both panchromatic cameras with a broadband response over the visible spectrum ( $\sim 400\text{--}700$  nm). Their boresights roughly point in the same direction as the OSIRIS-REx science instruments, away from the nadir deck, but have slight offsets to support operational pointing efficiency. The NavCam 1 and 2 boresights point approximately  $6^\circ$  and  $14^\circ$  off of the science instrument boresights, respectively. Twenty degrees separate the NavCam 1 and 2 boresights from each other. StowCam is sensitive to light across the same 400-700 nm band as NavCam 1 and 2 but includes a Bayer color filter (Bayer 1976) directly on the detector array to support color-interpolated imaging. StowCam's boresight is pointed at the SRC and almost exclusively views items on the spacecraft deck. The StowCam focus is optimized to image features on the spacecraft deck, whereas both NavCam focus positions are optimized for imaging at infinity. TAGCAMS is described in detail by Bos et al. (2018).

## 2 Observation Summary

During the OSIRIS-REx outbound cruise to Bennu we took advantage of an Earth fly-by and almost two years of unobstructed views of deep space to check and refine the TAGCAMS ground-based calibration. Although the TAGCAMS functionality and performance metrics had been tested and verified on the ground, in most cases the optimum environment for calibrating the instrument's performance proved to be deep space. The observations were

also motivated by our desire to confirm that the rigors of launch, radiation and extremes in temperature had not substantially altered the TAGCAMS performance.

We acquired a total of 1,183 TAGCAMS images for checkout and calibration during the spacecraft outbound cruise from September 22, 2016, to July 22, 2018 (Bos et al. 2019). The imaging activities consisted of nine campaigns:

- Launch +14 Day Checkout (September 22, 2016) 19 images;
- StowCam Spacecraft Outgassing Monitoring (March 2, 2017) 5 images;
- Launch +6 Month Calibration Part 1 (April 10-17, 2017) 385 images;
- Launch +6 Month Calibration Part 2 (June 12, 2017) 89 images;
- Launch +10 Month Checkout (August 3-4, 2017) 25 images;
- Earth Gravity-Assist (September 22-28, 2017) 108 images;
- OCAMS (OSIRIS-REx Camera Suite) Stray Light Ride-Along (January 18, 2018) 80 images;
- Launch +18 Month Calibration (March 8-22, 2018) 447 images;
- Launch +22 Month Checkout (July 22, 2018) 25 images.

The majority of the TAGCAMS cruise images captured were of star fields but also included resolved observations of Earth and the Moon, images of the SRC, and unresolved images of Solar System planetary bodies including: Mars, Jupiter, Earth and the Moon.

Most of the outbound cruise imaging activities produced data useful for TAGCAMS calibration and performance monitoring, with the exception of 39 NavCam 1 images acquired as part of the Launch +6 Month Calibration Part 1 campaign on April 16, 2017. Those images were completely saturated in the optically active portion of the images due to direct solar illumination of the camera's interior baffle surfaces. The images were unsuitable for their intended purpose of characterizing optical distortion at the expected high end of the camera's operational temperature. These measurements were successfully obtained later during the Launch +18 Month Calibration campaign but also necessitated the commencement of a concerted ground test effort using a NavCam 1 engineering model to better characterize scattered light performance.

The 921 images acquired as part of the Launch +6 Month Calibration Part 1, Launch +6 Month Calibration Part 2 and Launch +18 Month Calibration campaigns make up the primary TAGCAMS in-flight calibration dataset. One goal of those campaigns was to acquire NavCam 1 and 2 images at camera temperatures and temperature gradients similar to those predicted to occur during asteroid operations around Bennu. Through pre-observation thermal modeling, we discovered that this could not be achieved via manipulation of the camera and spacecraft heaters onboard the spacecraft, except in the case of the dark current and hot pixel calibration. To impart operations-like temperatures and temperature gradients for the calibration of camera pointing accuracy, pointing stability, magnification and optical distortion we had to develop a different approach.

To achieve the desired temperatures and temperature gradients we used spacecraft rotations that allowed sunlight to fall directly onto the spacecraft deck and TAGCAMS at particular angles. We then let the spacecraft and cameras warm up for at least half a day (14.8 hours during the Launch +6 Month campaign and 15.9 hours during the Launch +18 Month campaign) until temperatures and temperature gradients stabilized. After the desired thermal equilibrium conditions were achieved, we acquired images and rolled the spacecraft about the solar illumination vector to image different portions of the sky while maintaining the same solar illumination and thermal conditions. We used different spacecraft attitudes with different solar illumination to achieve measurements throughout the expected TAGCAMS asteroid operational temperatures of  $-30^{\circ}$  to  $10^{\circ}$  C.

### 3 Linearity and Point Source Responsivity

A key TAGCAMS performance parameter that we investigated during the outbound cruise phase of the OSIRIS-REx mission was the linearity of the NavCam 1 and 2 detectors. After delivery of the TAGCAMS to the OSIRIS-REx spacecraft in July 2015, subsequent performance analyses identified sporadic anomalies and inconsistent response linearity in the TAGCAMS detectors. An investigation traced these non-ideal characteristics to the detector register settings selected by the camera manufacturer and led us to select register settings more suitable for our application. We completed a coarse assessment of what we considered to be improved register settings during the spacecraft assembly, test and launch operations (ATLO) period but the first opportunity to more accurately confirm the linearity of the camera's response occurred after launch.

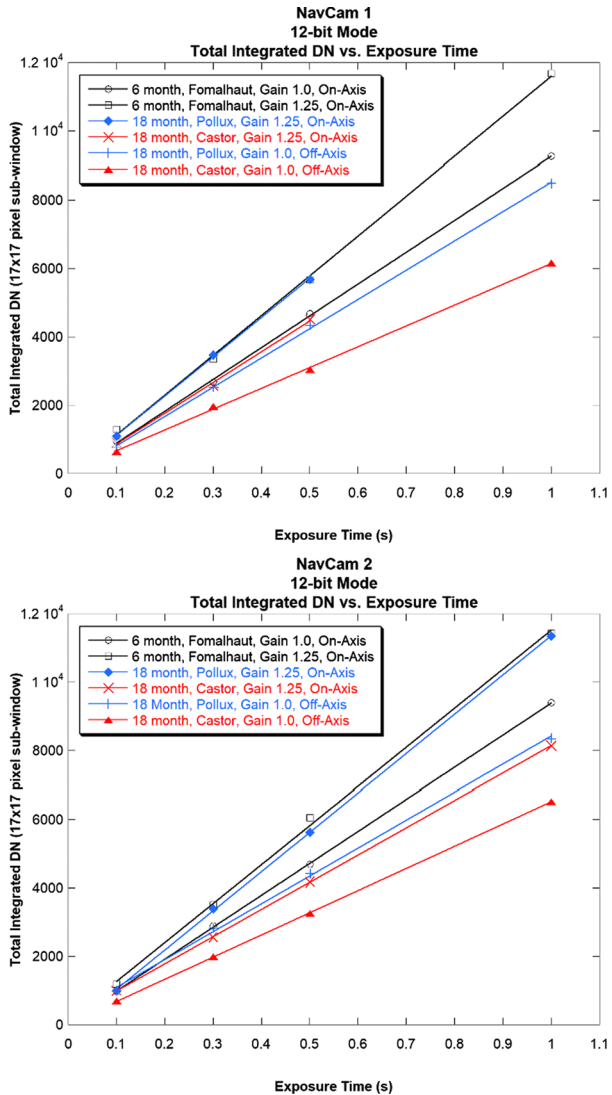
We acquired NavCam 1 and 2 linearity data during two days of the Launch +6 Month calibration campaign (April 10, 2017 and April 13, 2017) and one day during the Launch +18 Month calibration campaign (March 20, 2018). Camera head temperatures during these observations ranged from  $-26^{\circ}$  to  $-21^{\circ}$  °C, similar to the camera temperatures expected during most asteroid operations. For the Launch +6 Month observations, we selected the star Fomalhaut as the target. For the Launch +18 month observations, we selected Pollux and Castor. OSIRIS-REx's orbit precluded the ability to image identical stars during the two campaigns. We only tested the 12-bit mode linearity of NavCam 1 because it is the only mode we expect to use during asteroid operations. We tested both the 8-bit and 12-bit modes in NavCam 2. NavCam 2 typically operates in 8-bit mode when it acquires data to support NFT but operates in 12-bit mode if it supports optical navigation. During the Launch +6 Month calibration campaign, we only investigated the on-axis response linearity. For the Launch +18 Month observations, we investigated the on-axis and the off-axis response linearity ( $11^{\circ}$  from the center of the field of view along the long axis of the camera field of view and  $8^{\circ}$  from the center of the field of view along the short axis of the camera field of view). To acquire these sets of images the spacecraft held a constant attitude while acquiring star images using four different exposure settings (0.1, 0.3, 0.5 and 1.0 s) to test the camera dynamic range over one order of magnitude. We also commanded the acquisition of a fifth, 5-s image that would overexpose the core of the point spread function (PSF) but assist with selecting the integration window and estimating the detector saturation level. Although we originally pursued acquiring a larger sample of exposure times, resource constraints of the calibration campaign limited the number of exposures acquired.

After the images were downlinked, we reduced the data in five steps. First, we corrected the column-to-column variations caused by dark noise and the DN (digital number) offset by subtracting those effects that were recorded in the dark reference pixel area located at the periphery of the detector active area (see Fig. 6). Second, we examined the 5-s exposures and found that the PSF was well-contained within a  $17 \times 17$  pixel sub-window for the exposure times used. Third, we located the peak pixel in each of the Fomalhaut, Pollux and Castor images and centered a  $17 \times 17$  pixel sub-window on the peak pixels. Fourth, we calculated the total integrated DN values within the sub-windows for each star observed. Fifth, we calculated linear fits for the total integrated DN values versus exposure times by using root-sum-squares (Fig. 1).

Figure 1 shows the linear response of NavCam 1 in 12-bit mode and NavCam 2 in 8-bit and 12-bit mode over one order of magnitude in exposure time. For NavCam 1, the typical deviation from a linear fit was better than  $\pm 2.2\%$ , with the highest signal-to-noise measurements typically agreeing to a linear fit an order of magnitude better than that. The linearity results for NavCam 2 were slightly better with most of the deviations from a linear fit better than  $\pm 1.6\%$  in 8-bit mode and  $\pm 0.8\%$  in 12-bit mode. These deviations are consistent

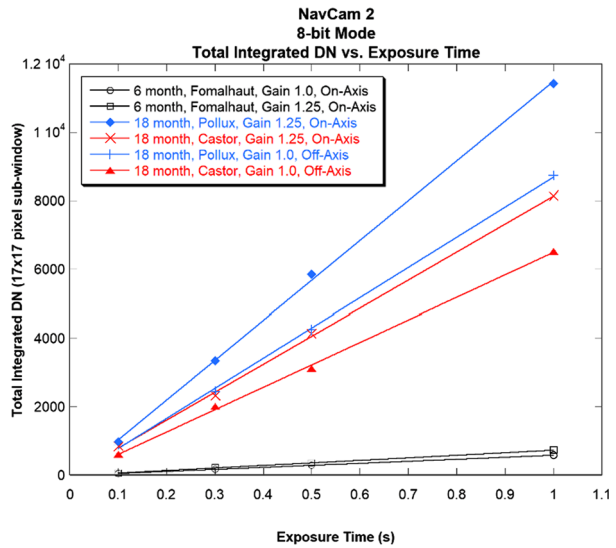


**Fig. 1** NavCam 1 and NavCam 2 response linearity to point-sources over a range of exposure times during the Launch +6 Month and +18 Month calibration campaigns, observing the bright stars Fomalhaut, Pollux and Castor. The top, middle and bottom plots are the responses for NavCam 1 operated in 12-bit mode, NavCam 2 operated in 12-bit mode, and NavCam 2 operated in 8-bit mode, respectively. The  $1\sigma$  error bars are equal to the diameter of the data symbols and are not plotted for clarity



with the  $1\sigma$  error estimate calculated from the variability of the non-illuminated pixels that surrounded the targeted stars.

The linearity results indicate the detector register setting changes improved the range of the cameras' linear responses from what they were at delivery. The demonstrated NavCam 1 and 2 linear ranges increased by 23% and 17%, respectively. We attribute the slight difference in the in-flight measurement of the two cameras' range of linearity improvement to the slightly better registration of the star targets on the NavCam 1 detector. We have no reason to believe that the detector register settings behave differently in the NavCam 1 and 2 detectors. Based on these results, for OSIRIS-REX asteroid operations we expect the cameras' responses will be linear to at least the 2% level,  $1\sigma$  over 97% of the detector's analog-to-digital converter range.

**Fig. 1** (Continued)

An unexpected result from the linearity calibration was the observed reduction in the slope of the linear fit for the off-axis observation of Castor compared with the on-axis observation by NavCam 1. We obtained the off-axis observations using a gain setting of 1.0 and the on-axis observations using a gain setting of 1.25, therefore, we expected a ratio close to 1.25 between the slopes of the two observations. But the slope ratio for the Castor observation was 1.47 – significantly larger than expected. Optical cosine effects account for some of the differences (the off-axis Castor observations were more than 13° away from the on-axis observations) but another effect had to be at play, so we investigated further.

All three TAGCAMS cameras use the same ON Semiconductor (formerly Aptina) MT9P031 5-megapixel complementary metal oxide semiconductor (CMOS) detector. This detector’s active pixels do not provide a 100% fill-factor. Some of the energy incident on the detector is lost in optically in-active locations between the pixel sites. Microscopic inspection of the detector pixels confirmed that the manufacturer-reported 2.2  $\mu\text{m}$  pixel pitch (or pixel-to-pixel spacing) was accurate to at least the second decimal point, but the optically active portion was less than the reported  $2.2 \times 2.2 \mu\text{m}^2$  pixel area, closer to  $1.43 \times 1.43 \mu\text{m}^2$ . To determine the effect that this has on the integrated flux that the detector measures, we completed a Monte Carlo simulation of the detection process to estimate the response variability.

To simulate the radiometric response of the camera we created a polychromatic PSF from the nominal TAGCAMS lens design and included both diffraction effects and design-residual aberrations. Individual wavelength responses were weighted by the reported quantum efficiency of the detector. We simulated the detector array with a grid of uniformly responsive  $1.43 \times 1.43 \mu\text{m}^2$  squares spaced every 2.2  $\mu\text{m}$  in two directions. We programmed the optical PSF to be randomly positioned over the detector array using a uniform probability distribution function; for each position realization the total energy within in each pixel was summed to create a simulated DN value at each pixel site. Then the simulation integrated the total DN value for a variety of sub-window sizes and stored those values for each realization. We found stability to the third significant digit using Monte Carlo runs with 100,000 trials. For a  $17 \times 17$  pixel sub-window, the  $1\sigma$  variation in integrated response was

found to be 6.0% due to photons going undetected between the pixel sites. This variation was large enough to account for the variability seen in the linear response data.

Because of the <100% fill-factor of the cameras' active pixels, and the size of the system PSF (the in-flight data indicates the system PSF full-width half-maximum on-axis is  $\sim 3 \mu\text{m}$ , see Sect. 8) with respect to the detector 2.2- $\mu\text{m}$  sampling period, the NavCam 1 and 2 imagers cannot produce high-accuracy photometry of stellar point sources. The broadband and non-uniform response over wavelength of the cameras also makes developing a highly accurate radiometric calibration difficult. But for asteroid operations purposes, we required a reasonably accurate calibration to predict the cameras' range of responses to stars to support stellar optical navigation planning. To acquire the point source responsivity calibrations for NavCam 1 and 2 we used data acquired during the Launch +14 Day Checkout period on September 22, 2016. These data included 1.6, 2.0 and 20 s observations in both cameras and contained a large number of catalogued stars within them. We used the Goddard Image Analysis and Navigation Tool (GIANT) (Wright et al. 2018) to autonomously identify the catalogued stars in the images and assign apparent magnitudes to them using the *v*-band from the UCAC4 (U.S. Naval Observatory CCD Astrograph Catalog) catalog. GIANT identified a total of 1,847 stars in the NavCam 1 images and 3,809 stars in the NavCam 2 images. A review of the GIANT results and images indicated that the larger number of stars in the NavCam 2 images was due to a larger portion of its field of view covered by the Milky Way.

To develop a calibration for the cameras' peak response to point sources we subtracted off the DN offset values from each pixel and centered a  $5 \times 5$  pixel sub-window at each star location identified by GIANT. We selected a  $5 \times 5$  pixel sub-window instead of a larger area to reduce the risk of light from closely adjacent stars affecting the integrated DN signal from the star of interest. The camera detector modeling described above indicated the  $1\sigma$  response variation for a  $5 \times 5$  sub-window was only 6.4%. Finally, we divided the total DN values by the image exposure times. Due to the base 10 logarithm relationship between star intensity and *v*-band apparent magnitude we fit these data via root-sum-squares to the function:

$$S(m) = c_1 10^{c_2 m}, \quad (1)$$

where  $S(m)$  is the signal in  $\text{DN/s}$ ,  $m$  is apparent magnitude and  $c_1$  and  $c_2$  are constants. For NavCam 1 we found  $c_1 = 31564.2$  and  $c_2 = -0.40362$ . For NavCam 2 we found  $c_1 = 23088.6$  and  $c_2 = -0.36177$ . Figure 2 shows the data and the corresponding fits.

Although the total integrated energy within a particularly sized sub-window has some utility, we were most interested in the ability to predict the cameras' peak pixel response to stars of a particular apparent magnitude, so that star center-finding would not be degraded by saturation or a low signal-to-noise ratio. To determine this, we used the camera detector model described above to compute the fraction of energy detected in a peak pixel with respect to the total energy captured in a  $5 \times 5$  pixel sub-window. To calculate the minimum fractional energy, we positioned the peak of the optical PSF on the diagonal between two pixels at the midpoint between their centers and integrated the energy in the peak pixel and the total energy in a  $5 \times 5$  pixel window centered on the peak pixel. To calculate the maximum fractional energy we completed the same calculation with the peak of the optical PSF centered on a pixel. We found the minimum peak pixel fraction to be 0.191 of the total and the maximum peak pixel fraction to be 0.574 of the total. To check the validity of the camera detector simulations, we re-analyzed our stellar observations and calculated the fractional energy in the peak pixel to the entire energy in a  $5 \times 5$  sub-window for each valid star that GIANT identified. The results indicate that the modeling provided a reasonable prediction of the large range in peak pixel responses (Fig. 3).

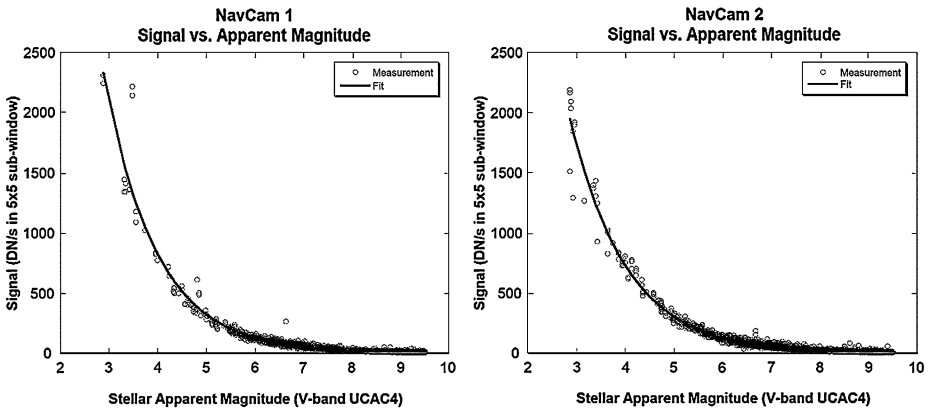


**Fig. 2** NavCam 1 (left) and 2 (right) stellar apparent magnitude signal results from the Launch +14 Day calibration campaign. The noise in the NavCam 1 results for stars dimmer than 7th magnitude caused us to ignore these stars in the fit, reducing the number of stars from 1,847 to 634. The noise in the NavCam 2 results for stars dimmer than 6th magnitude (likely due to the Milky Way) caused us to ignore these stars in the fit, reducing the number of stars from 3,809 to 366

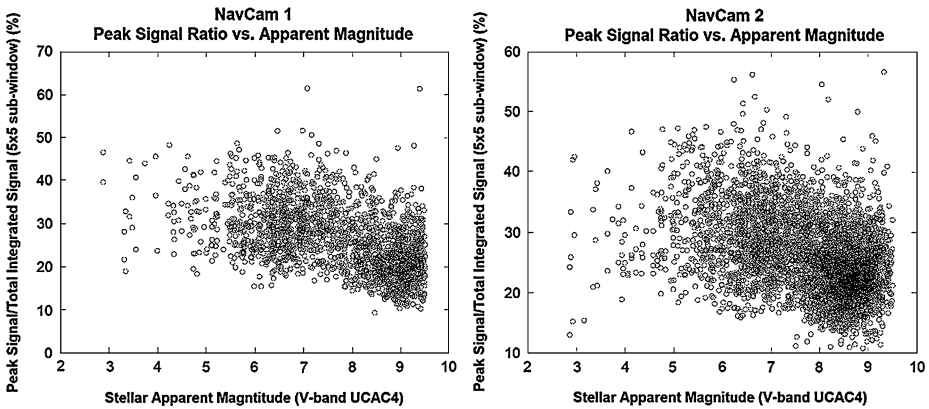


**Fig. 3** NavCam 1 (left) and 2 (right) peak pixel response ratios for the 1847 cataloged stars imaged with NavCam 1 and the 3809 stars imaged with NavCam 2. For NavCam 1 the variability data show good agreement with the range predicted by modeling of 19.1% to 57.4% up to approximately 7th magnitude where the stellar detections are questionable. For NavCam 2 the data show good agreement with the predicted range up to around 6th magnitude, where the stellar detections are noisier

Using this information, we developed the following equation to predict the 12-bit signal values for a given exposure time:

$$DN(t, m, g) = P c_1 \frac{10^{(c_2 m)}}{1.25} t g + DN_0, \tag{2}$$

where  $t$  is exposure time in seconds,  $g$  is the detector gain (typically 1.0 or 1.25),  $DN_0$  is the hardware DN offset (typically 169 to 171) and  $P$  is the fraction of energy in the peak pixel.  $P = 0.191$  when the minimum possible value is desired and 0.574 when the maximum possible value is desired.

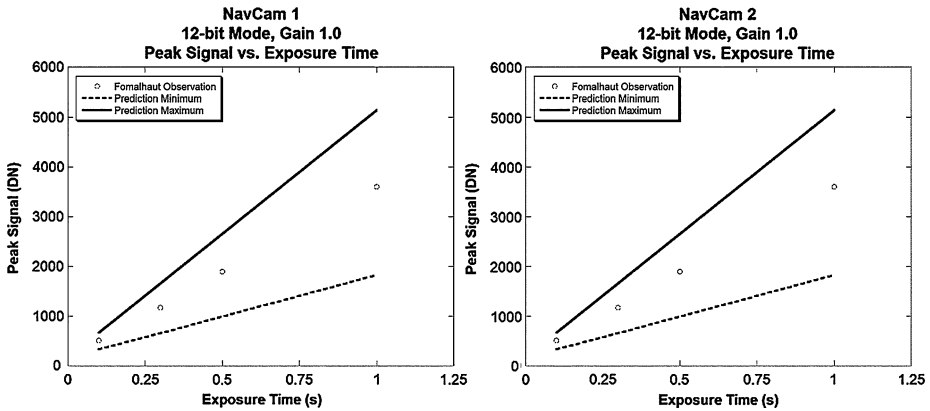


**Fig. 4** Examples of NavCam 1 (left) and 2 (right) peak pixel responses during the Launch +6 Month calibration observations of the bright star Fomalhaut. For the results shown above, the cameras operated in 12-bit mode with unity gain. The dashed lines show the minimum peak pixel values predicted by Eq. (2). The solid lines show the maximum peak pixel values predicted by Eq. (2). In both cases the predicted maximum peak pixel value exceeded the maximum value (4095 DN) of the analog-to-digital converter but the star was not perfectly centered on the pixel, so the measured peak pixel signal was within the 12-bit dynamic range of the cameras

We found the camera peak pixel response ranges specified by Eq. (2) to be accurate for exposure planning purposes throughout the entire outbound cruise phase of the OSIRIS-REx mission, and we did not observe any changes requiring recalibration. Figure 4 shows an example of the minimum and maximum peak pixel values predicted by Eq. (2) and how they compare to actual values in observations of Fomalhaut acquired during the Launch +6 Month calibration campaign. The plots in Fig. 4 illustrate the wide range of peak pixel values possible while observing a stellar or other unresolved target. We consider this wide range of possible peak pixel responses when planning stellar observations with NavCam 1 and 2. At times we choose to risk saturation to increase the chances of obtaining an image with a high signal-to-noise ratio and select exposure times that could result in peak pixel values that are at or are slightly above saturation (as we did for the 1-s observations of Fomalhaut shown in Fig. 4). Other times, we cannot tolerate any risk of saturating a particular object and choose exposure times that predict maximum peak pixel values that do not exceed or are safely below saturation. Due to the range of responses of the cameras to point sources, these considerations are necessary by planners any time a high-priority target is imaged.

## 4 Extended Object Radiometry

### 4.1 Introduction

During the OSIRIS-REx Earth-gravity assist (EGA) flyby maneuver, NavCam 1 and 2 acquired images of the sunlit disk of Earth positioned over the eastern Pacific. This provided an opportunity to validate the NavCam pre-launch calibration via radiometric inter-comparison with well-calibrated Earth viewing sensors. Satellite imagers in geostationary orbits are best suited to inter-calibrate the NavCam images because they offer frequent imaging of the same Earth disk location. The GOES-15 (Geostationary Operational Environmental Satellite 15) imager (Menzel and Purdom 1994), which is the Western United States' operational

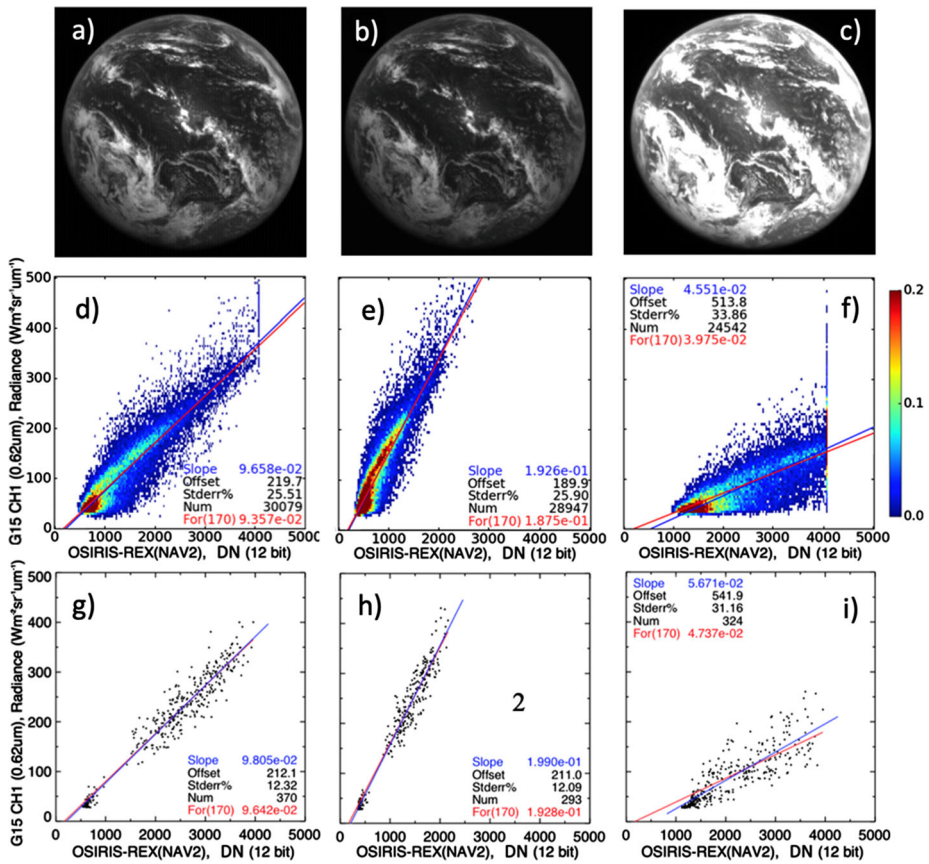


**Fig. 5** The NavCam 2 images taken September 22, 2017, at (a) 22:38:27 GMT, (b) 22:43:33 GMT and (c) 22:43:41 GMT. The exposure time of (b) is half that of (a), and the exposure time of (c) is about twice that of (a). The NavCam 2 DN at 4095 are considered saturated. The NavCam 2 DN at (d) 22:38:27 GMT, (e) 22:43:33 GMT, and (f) 22:43:41 GMT are shown with the 22:30 GMT GOES-15 pixel radiance collocated pairs, displayed as a relative density plot. The color scale is in relative frequency. Panels (g), (h), and (i) are the same as (d), (e), and (f), but for the ATO-RM pairs. “Slope”, “Offset” and “STDerr%” are the orthogonal linear regression gain, x-offset in DN, and associated standard error in percent, respectively. “Num” is the number of pairs for the month. “For” is the force fit gain or the linear regression through the NavCam 2 space DN of 170

weather satellite, is located at  $135^\circ$  West, and has the most similar field of view to the NavCam images. Accurately calibrated NavCam images not only help to optimize the NavCam exposure times, as there is no automated exposure feature on the NavCams, but also provide supplementary data on Benu’s albedo.

The inter-calibration approach process is as follows. First, the GOES-15 pixel-level image is reprojected into the NavCam fields of view. Coincident, collocated and ray-matched or bore-sighted pixel-level radiance pairs are then used to transfer the calibration from the GOES-15 reference sensor to the NavCam cameras. An all-sky tropical ocean ray-matching (ATO-RM) algorithm (Doelling et al. 2018) is applied that balances the degree of angle matching over the Earth observed radiance range without biasing the resulting gain. The ATO-RM algorithm also takes into account the GOES-15 and NavCam radiance differences

**Table 1** The NavCam image times calibrated in this study during September 22, 2017, in GMT. The NavCam 2 times are bold. The matched GOES-15 (FD, NH) image times are given in GMT. For GOES-15 the time is expressed at the equator. The GAM (VZA, RAA, SCAT) thresholds in degrees are shown for the top half and bottom quartile radiances. The NavCam gains ( $\text{Wm}^{-2} \text{sr}^{-1} \mu\text{m}^{-1} \text{DN}^{-1}$ ) based on the ATO-RM for radiances  $<200 \text{ Wm}^{-2} \text{sr}^{-1} \mu\text{m}^{-1}$  ( $<200$ ) are shown. The ATO-RM orthogonal regression standard deviation ( $\sigma$ ) in percent and x-offset (Off) in DN are shown in the last two columns

NavCam 1/2	GOES-15	GAM		Gain			
		Bright	Dark	ATO-RM	<200	$\sigma$	Off
21:10:54	21:13 FD	15,30,20	10,25,15	$1.0040 \times 10^{-1}$	$1.0080 \times 10^{-1}$	13.1	187
21:13:17	"	"	"	$1.0000 \times 10^{-1}$	$1.0050 \times 10^{-1}$	13.5	194
21:15:35	"	"	"	$1.0030 \times 10^{-1}$	$1.0080 \times 10^{-1}$	14.3	196
21:20:52	"	"	"	$1.0110 \times 10^{-1}$	$1.0150 \times 10^{-1}$	13.4	198
21:32:06	21:35 NH	15,30,20	15,30,20	$9.919 \times 10^{-2}$	$9.942 \times 10^{-2}$	11.6	115
21:35:26	"	"	"	$9.758 \times 10^{-2}$	$9.802 \times 10^{-2}$	10.8	137
21:37:41	"	"	"	$9.673 \times 10^{-2}$	$9.748 \times 10^{-2}$	10.4	185
22:04:32	22:05 NH	15,25,20	5,15,10	$9.638 \times 10^{-2}$	$9.687 \times 10^{-2}$	10.8	153
22:06:50	"	"	"	$9.676 \times 10^{-2}$	$9.716 \times 10^{-2}$	11.5	133
22:09:14	"	"	"	$9.680 \times 10^{-2}$	$9.716 \times 10^{-2}$	10.1	142
22:38:27	22:35 NH	25,30,15	15,20,5	$9.605 \times 10^{-2}$	$9.734 \times 10^{-2}$	12.3	212
22:43:33	"	"	"	$1.9130 \times 10^{-1}$	$1.9140 \times 10^{-2}$	12.1	211
22:43:41	"	"	"	$4.940 \times 10^{-2}$	$5.374 \times 10^{-2}$	28.7	541

attributed to the spectral response disparity. The three NavCam 2 images were taken at the time of the Earth flyby with a factor of  $\pm 2$  exposure times, thereby offering a chance to validate the ATO-RM algorithm over a wide range of exposure times (Fig. 5a, b, c). To facilitate a direct comparison between the pre-launch and ATO-RM calibrations of the cameras, a correction factor is derived to account for the difference in using the Earth-reflected solar spectra for ATO-RM versus a lamp spectra for pre-launch calibration. Doelling et al. 2019 contains a more extensive study of the ATO-RM based in-flight calibration of the NavCam sensors (Doelling et al. 2019).

## 4.2 ATO-RM Inter-Calibration Methodology

We used ten NavCam 1 and three NavCam 2 images that were acquired during the September 22, 2017 OSIRIS-REx Earth EGA flyby maneuver for inter-calibration. The acquisition times for these images are listed in Table 1. The NavCam 1 and 2 CMOS detector arrays consist of a 2592 by 1944-pixel optically active area,  $\sim 350 \times 350$  pixels were covered by Earth and have a nominal pixel scale of  $\sim 34$ -km. The NavCam cameras have a broad visible spectral response ( $0.4 \mu\text{m}$  to  $0.7 \mu\text{m}$ ). Table 1 lists the one full disc (FD) and three Northern Hemisphere (NH) GOES-15 images that were coincident during the flyby maneuver along with the NavCam image pairings. Because the GOES-15 imager does not have any onboard calibration systems, the GOES-15 pixel-level radiances are first tied to the radiometric scale of the well-calibrated Aqua-Moderate Resolution Imaging Spectroradiometer (MODIS) band 1 ( $0.65 \mu\text{m}$ ) reference. Aqua-MODIS is a polar orbiting environmental sensor with an onboard solar diffuser to monitor the inflight calibration (Xiong and Barnes 2006). The GOES-15 visible channel has a narrow spectral response function of  $0.5 \mu\text{m}$  to  $0.7 \mu\text{m}$ . We mapped the 4-km GOES-15 pixels into the NavCam active-pixel field of view.



We then aligned the reprojected GOES-15 image with the NavCam images to collocate the cloud features.

The ATO-RM algorithm matches the GOES-15 and NavCam collocated pixels in time, in wavelength, and by viewing and solar conditions. The ATO-RM algorithm relies on the full range of Earth viewed radiances that are observed over the tropics. Land regions are avoided due to their unique spectral signatures. The GOES-15 radiances are adjusted to match the NavCam spectral response function by applying a spectral band adjustment factor (SBAF) (Chander et al. 2013). The Earth-reflected spectrum is a function of the incoming solar irradiance and the reflectance properties of the surface and cloud conditions. Except for deep convective clouds, the Earth-reflected radiances are not spectrally flat. The SBAF's are based on SCIAMACHY (SCanning Imaging Absorption spectroMeter for Atmospheric CHartographY) hyper-spectral observed radiances that resemble the Earth-viewed ATO conditions and are computed from the NASA-Langley SCIAMACHY-based SBAF tool (Scarino et al. 2016). The degree of viewing and azimuthal angle matching is dependent on the underlying surface and cloud conditions. Bright cloud targets are more Lambertian than the darker clear-sky and partly cloudy ocean targets. Therefore, a strict angle matching is required over dark targets, whereas over bright targets broad angle matching is sufficient. Fortunately, the frequency of dark targets is much greater than bright targets. A graduated angle matching (GAM) is applied to preserve the dynamic range of Earth viewed radiances (Doelling et al. 2016). To avoid oblique views, GAM limits the view zenith angle to  $40^\circ$ . GAM applies angle matching thresholds in three steps across the radiance range: 1st and 2nd quartiles, and the combined 3rd and 4th quartiles. The NavCam images were paired with GOES-15 images that were closest in time. For each GOES-15 image, the GAM thresholds were adjusted to obtain sufficient sampling over the radiance range. A pixel-level homogeneity filter of 0.2, computed from the standard deviation of the surrounding 8 pixel-level radiance divided by the mean, was also applied to mitigate the impact of navigation errors, pixel resolution differences and complex cloud conditions. We also normalized the GOES-15 radiances to match the NavCam solar zenith conditions to minimize the effect of any temporal difference in the ray-matched dataset.

### 4.3 ATO-RM Validation

All collocated GOES-15 radiances and NavCam 2 12-bit pixel-level DN pairs are illustrated as a density plot in Fig. 5d. The pre-launch and in-flight calibrations verified that the sensor response is linear. However, the radiance pairs have a non-linear feature, which is mostly due to the angular differences of the radiance pairs. Two linear regressions were used to quantify the robustness of the angle matching. The force fit linear regression relies on the observed space DN offset of 170 to compute the gain, whereas the orthogonal linear regression estimates both the gain and offset. Figure 5d indicates that the gain and offset DN difference is 3.2% and 51, respectively. After applying ATO-RM, the gain and offset difference is 1.7% and 43 (Fig. 5g). The standard error has been reduced from 26% to 12%, thus verifying that angle matched radiance pairs are more linearly correlated.

Table 1 reveals that the NavCam 1 ten image linearly regressed average offset is 164, which is very close to the true offset of 170. To test the gain linearity over the radiance range, we computed another force fit gain using only bright radiances. The NavCam 1 ten-image ATO-RM and bright radiance average force fit gain difference was 0.4%, indicating that GAM thresholds are adequate. For each set of NavCam images assigned to a single GOES-15 image, we computed the ATO-RM gain standard deviation. As the GAM thresholds increased for the GOES-15 22:05 GMT, 21:13 GMT and 21:35 GMT images,

the ATO-RM gain standard deviations increased from 0.2% to 0.5% to 1.3%, respectively. As expected, stricter angular matching resulted in more accurate ATO-RM gains. The Earth location varied across the sequence of NavCam images. The small gain differences computed over the sequence of images imply that the NavCam CMOS detector array response uniformity is very good over the regions of the field of view tested.

The three NavCam 2 images provided the opportunity to test the ATO-RM algorithm across a factor  $\pm 2$  exposure times. Figures 5a, b, and c) were taken with exposure times of 0.1528 ms, 0.0764 ms, and 0.3228 ms, respectively. Figure 5a has  $2.0\times$  the exposure time of Fig. 5b, whereas Fig. 5a's exposure time is  $0.48\times$  that of Fig. 5c. The collocated GOES-15 radiance and NavCam 2 DN pixel pair density plots are shown in Fig. 5d, e, and f. Figure 5h shows half the NavCam DN range of Fig. 5g, yet the standard error of the linear regression and offset are very similar, and the force fit gain equals  $2.0\times$  of the gain in Fig. 5g. Figure 5f shows twice the DN range of Fig. 5d, where the bright cloud DN are saturated and are not useful for ATO-RM. The standard deviation and offset in Fig. 5i are similar to those in Fig. 5f. Without the bright cloud pixel pairs, the force fit and linear regression gains diverge, and the force fit line does not transect the dark pixel radiance pairs (Fig. 5i). However, the ATO-RM force fit, which relies on the observed space DN offset of 170, is able to capture a responsivity that is within 3.9% of the responsivity in Fig. 5g. Thus, the ATO-RM is well suited to provide accurate gains over exposure times that differ by a factor of  $\pm 2$ .

#### 4.4 Comparison with Pre-Launch Calibration

We characterized the NavCam 1 and 2 pre-launch radiance responses using an integrating sphere illuminated by a quartz-tungsten halogen (QTH) lamp, which had a peak radiance at  $\sim 1\ \mu\text{m}$ . The radiometric calibration for NavCam 1 and 2 was  $100,965\ (\text{DN/s})/(\text{Wm}^{-2}\ \text{sr}^{-1})$  and  $102,685\ (\text{DN/s})/(\text{Wm}^{-2}\ \text{sr}^{-1})$ , respectively. The pre-launch calibration computed the responsivity in the units of integrated in-band radiance.

The mean ATO-RM gains for the ten NavCam 1 images and the first NavCam 2 image (with an exposure time of 0.1528 ms) were computed to be  $9.874 \times 10^{-2}\ \text{Wm}^{-2}\ \text{sr}^{-1}\ \mu\text{m}^{-1}\ \text{DN}^{-1}$  and  $9.642 \times 10^{-2}\ \text{Wm}^{-2}\ \text{sr}^{-1}\ \mu\text{m}^{-1}\ \text{DN}^{-1}$ , respectively. Independent sources of uncertainties were quantified and summed in quadrature to compute the total uncertainty of the ATO-RM calibration. The Aqua-MODIS band 1 ground to orbit calibration uncertainty is 1.65% (Xiong 2011) and the MODIS on-orbit calibration drift uncertainty is estimated at 1% (Doelling et al. 2015). The GOES-15 and Aqua-MODIS inter-calibration uncertainty is 1.1%. The GOES-15 and NavCam 1 SBAF uncertainty is estimated to be 1.9%. The ATO-RM gains for the ten NavCam 1 images exhibit a standard deviation of 1.8%. The resulting total uncertainty of the ATO-RM gain is estimated at 3.4%.

We used the derived ATO-RM gains to convert the NavCam DN to spectral radiance units. For direct comparison with the pre-launch values, the ATO-RM gains must be adjusted for spectral radiance to in-band radiance conversion, normalized by the exposure time, and corrected for the difference in the input reference spectra used in the two methods. We multiplied the ATO-RM gains by the equivalent width ( $0.342\ \mu\text{m}$ ) of the NavCam sensor pass band to convert the units of the responsivities from spectral radiance to in-band radiance. Next, we inverted the responsivities and divided by the image exposure time of 0.1528 ms to match with the conversion units of the pre-launch gains. The ATO-RM gain was based on the Earth reflected solar spectra and was corrected to resemble the QTH lamp spectra used for the pre-launch calibration. We calculated a correction factor of 0.5337, based on the ratio of the in-band sensor response to the total over the pass band input radiance computed for each reference spectra. The ATO-RM spectra was based on the mean footprint

of SCIAMACHY hyper-spectral radiances observed over ATO conditions. After applying the reference spectra correction factor, the NavCam 1 and 2 ATO-RM gains were 103,129 (DN/s)/(Wm<sup>-2</sup> sr<sup>-1</sup>) and 105,610 (DN/s)/(Wm<sup>-2</sup> sr<sup>-1</sup>), respectively. The ATO-RM and pre-launch gains were within 2.14% and 2.8% for NavCam 1 and 2, respectively, and within the ATO-RM gain uncertainty. The responsivity ratio between NavCam 1 and 2 for pre-launch and ATO-RM was 0.9833 and 0.9765, respectively, which is consistent within 0.7%.

## 4.5 Extended Object Radiometry Conclusion

We found that the NavCam 1 and NavCam 2 on-orbit responsivities agree well with the pre-launch extended body responsivity calibration. The ATO-RM responsivity we calculated was within 2.8% of the pre-launch values, which is within the predicted ATO-RM responsivity uncertainty. This result indicates that the OSIRIS-REx launch and the 379 days spent in space between the launch and the Earth flyby did not meaningfully alter the NavCam 1 and 2 responsivities. This work also suggests that the ATO-RM calibration approach can easily calibrate Earth images observed by any planetary probe.

## 5 Dark Current Calibration and Hot Pixels

### 5.1 Dark Current

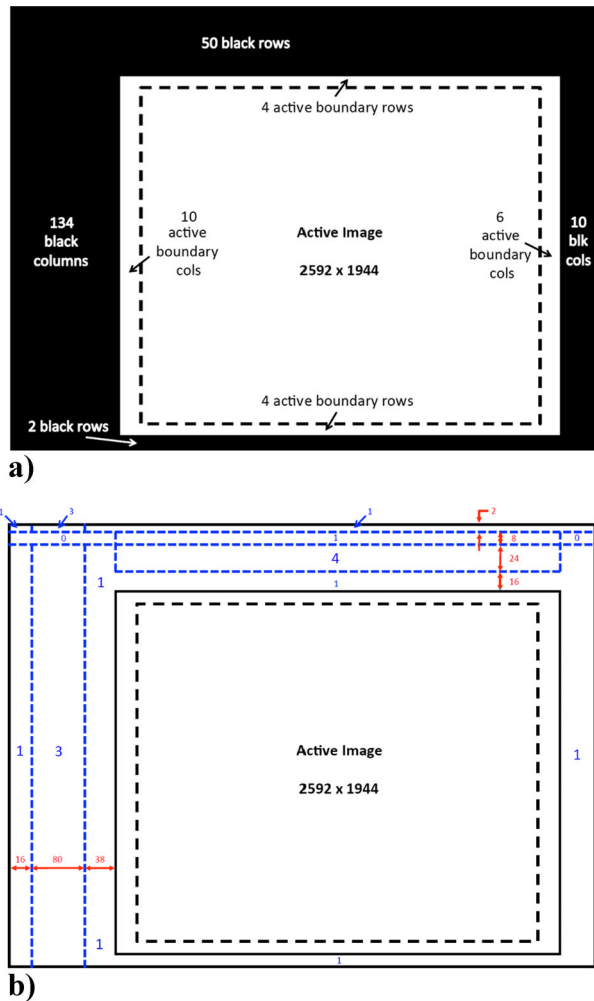
NavCam 1 and 2 ground testing indicated that detector dark current would be a negligible contributor to image noise for the exposure times planned for operations (longest expected is 2 s, whereas the longest currently allowed by software timing is 20 s). Read noise is expected to dominate all the noise terms. For instance, at -25 °C, with a 1-s, 12-bit exposure using a gain setting of 1.0, we expect 0.006 to 0.018 e<sup>-</sup> of dark current compared to a read noise of 6.7 e<sup>-</sup>. Increasing the detector temperature to 10 °C increases the dark current to 0.22 to 0.66 e<sup>-</sup> but is still smaller than the quantization step size of the 12-bit analog-to-digital converter. Our ability to measure dark current onboard the spacecraft is severely limited due to the low signal-to-noise ratio of the dark current signal and the maximum 20 s exposure constraint.

Even though we expect the dark current to remain negligible when OSIRIS-REx asteroid operations commence, we know continuous exposure to the space environment over the currently planned 3.82 years from the time of launch to asteroid sample acquisition will inevitably cause the dark current rate to increase due to radiation damage. None of the three TAGCAMS camera heads include a mechanical shutter to shield the camera detectors from ambient light. This makes it inconvenient to characterize dark current during normal cruise operations. To facilitate monitoring of the NavCam 1 and 2 detector dark current we primarily relied on dark reference pixels located on the detectors.

In addition to the 2592 × 1944 optically active portion in each of the three TAGCAMS CMOS arrays, additional reference pixels are located around the periphery of the arrays, bringing the total number of electrically active pixels to 2752 × 2004 in each camera. Most of those additional pixels are located beneath an optically opaque substrate. Although the detector manufacturer's description of the functionality for most of the reference pixels lacks sufficient detail to support quantitative image calibration or correction, we have been able to use the limited information along with supplemental laboratory tests to determine some reference pixel functions. Figure 6 shows the pixel layout of the TAGCAMS detectors.

Region 4 is the reference pixel region of interest for characterizing detector dark current. We call pixels in this region the dark reference pixels. Each of the 62,208 dark reference

**Fig. 6** Diagram of the TAGCAMS detector pixel layout. Panel (a) shows the  $2592 \times 1944$  optically active portion of the detector and a general description of the pixels that make up the rest of the  $2752 \times 2004$  pixel array provided by the detector manufacturer. Panel (b) shows our interpretation of the reference pixel areas and the identification (ID) numbers 1 through 4 that we have assigned to those areas based upon our understanding of their function. The black borders represent the standard array boundaries as presented in (a), the blue borders and text represent the dark pixel region boundaries and region ID numbers, and the red annotations represent the dark pixel region dimensions in units of pixels. For our purposes, the  $2592 \times 24$  reference pixel region 4 is of particular interest. Those pixels respond electrically in the same fashion as the active image pixels but are covered by an optically opaque substrate and can therefore serve as dark reference pixels for assessing DN offset and dark current



pixels lie below an optically opaque substrate and each records the summation of the DN offset with the dark current. If commanded, they can be readout with each image exposure; this was done for each of the NavCam 1 and 2 images acquired during outbound cruise to generate a record of dark current over time and temperature.

In addition to the dark current measurements recorded in the dark reference pixels, we added a small number of follow-on observations near the galactic poles during the Launch +6 Month and Launch +18 Month calibration campaigns. Those observations checked the dark current in the optically active portion of the detector array to investigate the dark current behavior of those pixels with respect to the dark reference pixels. During those observations the camera heaters were activated to force the camera head temperatures to reach approximately  $10\text{ }^\circ\text{C}$ , the high end of the temperatures expected during asteroid operations. Even though we imaged portions of the sky with low densities of stars to ensure that signals from uncatalogued sky objects would not be mistaken for dark current, we implemented a specific imaging scheme to assist in reducing the odds of this occurring even further. The spacecraft acquired three images at one pointing attitude, slewed  $3^\circ$  along the short axis of a camera's

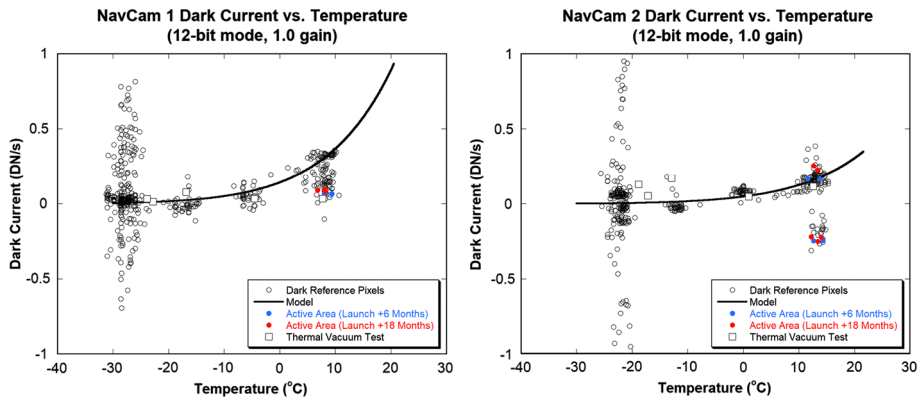


**Fig. 7** NavCam 1 (left) and NavCam 2 (right) plots of dark current observations versus camera head temperature. The open circles represent measurements from the dark reference pixel portion of the array. The solid, colored circles represent dark current measurements from the optically active portion of the array. The open square symbols represent spacecraft-level thermal vacuum test results. The solid lines show the best-fit model using Eq. (3). During operations our longest exposure time is expected to be 2 s. These data indicate that the dark current signal in a 12-bit image for a 2-s exposure will not exceed 1 DN, inconsequential to the image noise when considering the 0-4095 DN range of 12-bit imaging. The non-physical, negative dark current results are caused by noise in the DN offset and dark current estimates which are almost of identical value

field of view and took three more images, slewed back to the original attitude, and then slewed  $3^\circ$  along the long axis of a camera's field of view and took a final set of three images. This allowed us to easily remove signals from the data that were not due to dark current by comparing pixel signal values at all three pointing positions.

Figure 7 shows the dark current results in terms of DN/s for all the dark current data acquired during the outbound cruise phase of the mission for a gain of 1.0 in 12-bit mode. Most of the dark current results suffer from low signal-to-noise ratios - a consequence of the temperatures and exposure times. In addition, the dark current ground test results from the spacecraft-level thermal vacuum test period are included in the plots for comparison with the in-flight results.

One aspect of the plots in Fig. 7 that stands out is the large spread in results at cold temperatures. This is primarily due to the large amount of data that were acquired at those temperatures over a variety of exposure times. At cold temperatures the dark current is essentially zero but small noise sources can cause a pixel value to vary by a few DN. The apparent continuous range in the DN/s dark current rates at cold temperature is caused by the variety of exposure times used for the observations.

Even though the dark current data are noisy, we can draw several important conclusions from the dataset. The first is that the dark current signal is expected to be extremely low for all the exposure times and temperatures we expect to use during asteroid operations. Our longest exposures are expected to be 2 s and most of the time we will operate at the cold end of our operational temperature range, roughly  $-25^\circ\text{C}$ . These conditions should produce much less than 1 DN of dark current signal in 12-bit mode. Even at the hot end of our operational temperature range, approximately  $10^\circ\text{C}$ , a similar exposure still only generates about 1 DN of dark current signal in 12-bit mode.

Another important conclusion that we can draw from the dark current data is that the dark current response of the dark reference pixels is in-family with the response of the pixels from the optically active portion of the array. The dark reference pixels can serve as

a suitable surrogate for monitoring the dark current in the active portion of the array during asteroid operations. By comparing the in-flight dark current results to the spacecraft-level thermal vacuum test results we see no obvious change in dark current performance to within the noise of the measurements.

## 5.2 Dark Current Rate of Change

To further investigate whether any change in the dark current rate occurred after launch, we fit a dark current model to the data. The model we used was a derivation of the Bos (2002) model for calibrating dark current in Mars lander charge-coupled devices (CCD) but modified for the TAGCAMS CMOS detectors operated in 12-bit mode and is described by

$$DN(t, T, g) = gA_D t (T - \Delta_T)^{\frac{3}{2}} e^{\left(\frac{-E_g(T)}{2k(T-\Delta_T)}\right)} + DN_0, \quad (3)$$

where the pixel signal,  $DN$ , depends on the camera gain setting  $g$ , the exposure time  $t$  in seconds and the temperature  $T$  in Kelvin.  $\Delta_T$  is the difference between the detector silicon temperature and the temperature at the location of the temperature sensor on the detector board (and recorded in the TAGCAMS image headers).  $DN_0$  is the hardware DN offset.  $A_D$  is proportional to the dark current rate in DN/s/K<sup>3/2</sup>.  $E_g(T)$  is the temperature dependent silicon bandgap energy and  $k$  is Boltzmann's constant in eV/k. The silicon bandgap energy dependence on temperature we used was given by Pankove (1971) as

$$E_g(T) = 1.1557 - \frac{7.021 \times 10^{-4} T^2}{1108 + T}, \quad (4)$$

where  $T$  is again temperature in Kelvin. We fit Eq. (3) to the dark current data by minimizing the root-sum-square difference and assuming initial values for  $\Delta_T$  and  $DN_0$  of 0 K and 169 DN respectively. The best-fit for NavCam 1 found  $A_D = 714,916$  DN/s/K<sup>3/2</sup>,  $\Delta_T = 1.1029$  K and  $DN_0 = 169.64$  DN. The best-fit for NavCam 2 was  $A_D = 226,648$  DN/s/K<sup>3/2</sup>,  $\Delta_T = -0.04422$  K and  $DN_0 = 170.63$  DN. We attribute the factor of three difference between the  $A_D$  fits for NavCam 1 and 2 to the noise in the dark current data and likely not to differences in camera performance. The difference is driven primarily by the fraction of high-temperature results for NavCam 2 that have a slightly lower DN offset or dark current than most of the NavCam 2 results and lie noticeably below the 0 DN/s dark current rate in Fig. 7. Given the noise in the data we consider the dark current model fits to only provide an approximate estimate for the dark current generation rate. The model fits are plotted for each camera in Fig. 7.

Using the dark current model fits, we removed the temperature dependence from the dark current measurements to investigate any time-dependent trends that would indicate dark current rates different from the ensemble average. Figure 8 shows the differences between the model fit and the data as a function of spacecraft clock time.

Considered in their totality the data shown in Fig. 8 do not indicate an increase in dark current over time. But there may be some tenuous evidence for a slight increase at about the level of the noise in the results if the Launch +14 Day, Launch +10 Month and Launch +22 Month checkout images are considered in isolation (circled in red in Fig. 8). Those observations are particularly interesting because: they cover the greatest period of time, were taken at roughly the same temperature, and used long exposure times of 1.6, 2.0 and 20 s. Linear fits to those data suggest a slight dark current increase in time of 0.03 DN/s/year for NavCam 1 and 0.08 DN/s/year for NavCam 2. NavCam 1 and 2 use identical types of

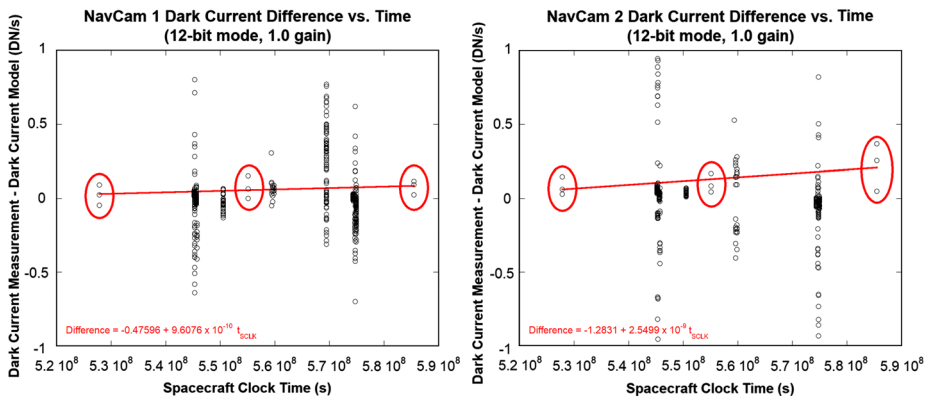


**Fig. 8** NavCam 1 (left) and 2 (right) plots of dark current rate deviation from the model fits versus time. The data are clustered in columns due to the acquisition of the observations during the discrete checkout and calibration periods described in Sect. 2. Because of the spread in the data, it is difficult to identify any trends over time by looking at the dark current results in their totality. Circled in red are the results for the Launch +14 Day, +10 Month and +22 Month checkouts. These images were acquired at roughly the same temperature with exposure times of 1.6, 2 and 20 s. A linear fit to those data alone indicate a dark current rate increase of 0.03 DN/s/year for NavCam 1 and 0.08 DN/s/year for NavCam 2

detectors, their camera heads are identical in material and design and are mounted adjacent to each other on the spacecraft deck. We wouldn't expect any appreciable differences in dark current performance between the cameras. We attribute the difference in the dark current rate of change between the two cameras to the noise in the results.

For another check on the change in dark current over time, we explored fitting a line to the data shown in Fig. 8 that included only those points where the exposure time was  $\geq 1.6$  s. Those exploratory fits indicated a reduction in dark current with time,  $-0.04$  DN/s/year for NavCam 1 and  $-0.05$  DN/s/year for NavCam 2. A final exploratory linear fit that included only data with exposure times  $\geq 1.6$  s and temperatures  $\geq 0$  °C also pointed to a reduction in dark current over time with the same order of magnitude. We know this is physically implausible and lends further credence to the idea that the dark current noise is a small contributor to the total noise in the data acquired during outbound cruise.

Even though we can only consider the dark current rates of change calculated from the checkout data as rough, not-to-exceed estimates, they are useful to help assess the qualitative likelihood of dark current degrading imaging performance at the time of the asteroid sample acquisition. The necessary rate of dark current growth to make the dark current noise equal to the camera read noise, currently the dominate detector-based noise term, is 3.24 DN/s/year. This is  $\sim 41$  times greater than the worst rate we observe in the checkout data.

We conclude that our pre-launch assessment of the dark current's impact on image quality is valid. Dark current will not significantly degrade NavCam 1 and 2 images during asteroid operations.

### 5.3 Hot Pixels

We analyzed the same dataset described in Sect. 5.1 to check for hot pixels in the optically active portions of the detector arrays acquired during the Launch +6 Month and Launch +18 Month calibration campaigns. We used the image noise statistics from that dataset to select the algorithm intensity threshold for considering a pixel value to be anomalously high



or a “hot” pixel. The pixel intensity threshold that we selected was 450 DN (in 12-bit mode) for a 2 s exposure, which was  $\sim 30\sigma$  greater than the mean noise plus hardware offset. This criterion reduced the probability to  $<0.0001$  that random noise alone would generate even one candidate hot pixel from the population of 5,038,848 optically active pixels. In addition, pixel values above 400–500 DN (in 12-bit mode) might be identified as potential stars by some of our star-finding algorithms and so cataloging hot pixels with that signal level seemed appropriate.

The second criterion the algorithm used to categorize an anomalously responsive pixel was persistence above the  $30\sigma$  threshold in all nine of the camera images acquired over the three different camera-pointing positions.

Using those criteria, the algorithm identified 194 hot pixels in NavCam 1 from the Launch +6 Month calibration campaign and 264 hot pixels from the Launch +18 Month calibration campaign. It found that NavCam 2 had 183 hot pixels in the Launch +6 Month calibration data and 294 hot pixels in the Launch +18 Month calibration data. Further processing determined that only about one-quarter to one-third of the hot pixel candidates matched between the two calibration campaign datasets. NavCam 1 had 64 pixels in common and NavCam 2 had 94.

Hot pixel populations of a few hundred (or even a few thousand) scattered across the camera fields of view are not of any concern to the primary users of the NavCam 1 and 2 images. The OSIRIS-REx optical navigation algorithms ignore pixel locations that do not match cataloged star locations. The NFT algorithm that supports the sample acquisition is also not very sensitive to individual spurious pixel responses. We only become concerned about the impact of hot pixels on NFT products if the hot pixels start to cluster into groups that might be mistaken for an extended object on the target asteroid’s surface. We investigated the location of the persistent hot pixels in NavCam 1 and 2 to see whether any of them neighbored each other.

We did not find any pixels in NavCam 1 with any form of connectedness (four or eight-sided) but we did identify two pixels in NavCam 1 that were only separated horizontally by one pixel. In that case, a new hot pixel that occurs in one of three pixel locations would convert that into a three-pixel region with eight-sided connectedness. For NavCam 2 we found one pair of hot pixels connected along a diagonal (i.e. eight-sided connectedness). From the perspective of Fig. 6, those two pixels are located halfway up the field of view and to the left of the center of the active portion of the array, about halfway in between the field of view center and the boundary pixels on the left. Although a two-pixel grouping is not of concern to NFT processing, the grouping’s location is in a prime portion of the field of view, so we will continue to pay particular attention to that portion of the field of view to see if any other pixels develop spurious responses. We expect to acquire images during asteroid operations for that purpose.

## 6 Boresight and Pointing Temperature Dependence

### 6.1 Overview

Although we measured the camera alignments before launch, we calibrated NavCam 1 and 2 in-flight to determine camera attitude pointing and alignment with respect to the spacecraft frame with higher accuracy. We used images of stars acquired during the outbound cruise to determine each camera’s attitude at each image epoch. Then we compared the camera attitude solutions to the camera attitude as determined by the spacecraft’s on-board attitude

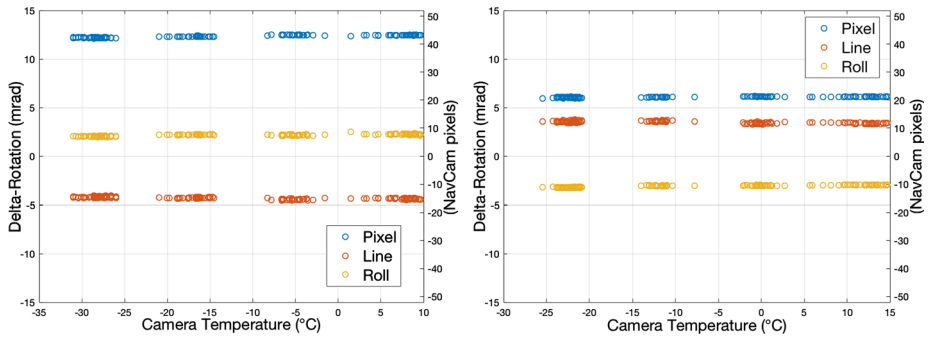


**Fig. 9** NavCam 1 (left) and 2 (right) alignment error as a function of camera temperature when using the pre-launch spacecraft-to-instrument rotation matrix. The left vertical-axis is in units of milliradians and the right vertical axis is in units of NavCam pixels (one NavCam pixel approximately 0.28 milliradians)

determination and control system (ADCS). The ADCS uses the spacecraft's star trackers and gyros to determine the spacecraft attitude, then uses the spacecraft-to-instrument frame transformation matrix, a pre-defined rotation matrix that describes the offset between the camera frame and the spacecraft frame, to determine the corresponding camera attitude at that epoch. This spacecraft-to-instrument matrix was initially slightly inaccurate, due to limitations of the initial ground calibration, resulting in a constant bias between the ADCS camera attitude solution and the solution determined using the star field images. To calibrate the alignment using the star field images, we estimated a new spacecraft-to-instrument matrix for each camera in a least-squares sense to minimize the difference between the ADCS camera attitude and star field attitude solutions. The residuals resulting from this least-squares solution show that the alignments of both cameras exhibit a slight temperature dependence.

## 6.2 Primary Analysis

We express the differences measured between the two attitude solutions here as delta-rotations defined by three Euler angles. We selected the axes for these Euler angle rotations such that the first rotation is about the instrument Y-axis (which corresponds to an offset along the long axis of an image). The second rotation is about the instrument X-axis (which corresponds to an offset along the short axis of an image). The third rotation is about the instrument Z-axis, representing the camera roll about its own boresight. We denote these three Euler angles as “pixel,” “line” and “roll,” respectively.

Figure 9 shows the error in the camera frame alignment for NavCam 1 and 2 before correcting the spacecraft-to-instrument rotation matrix with in-flight calibration images. As described above, this shows a constant bias for all three angles as a result of an a priori misalignment. The left vertical-axis is in units of milliradians and the right vertical-axis is in units of NavCam pixels (one NavCam pixel is approximately 0.28 milliradians).

Figure 10 shows the effect of updating the spacecraft-to-instrument rotation matrix using the in-flight calibration data, considerably reducing the alignment error. The results exhibit a possible slight temperature dependence in the alignment of both cameras, however the potential effect is about at the level of the spread in the results and could be due to noise. In addition, this alignment error is less than one pixel over the expected operational temperature range. This potential small amount of pointing change with temperature is acceptable for the mission's navigation purposes and therefore we use a static spacecraft-to-instrument alignment matrix independent of the NavCam 1 and 2 temperatures.

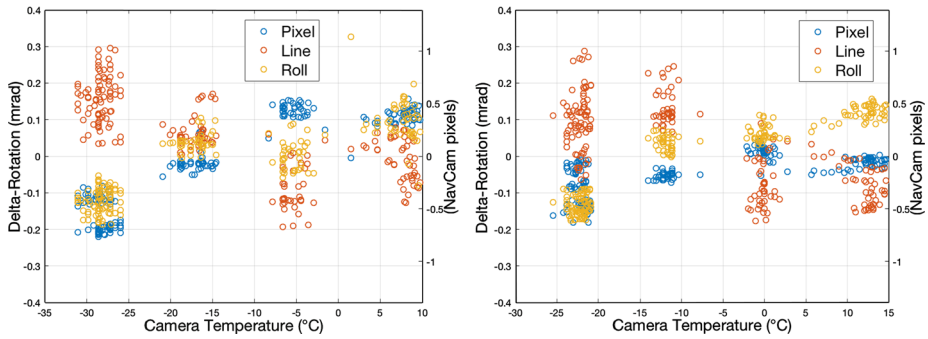


**Fig. 10** NavCam 1 (left) and 2 (right) alignment error as a function of camera temperature when using the in-flight calibrated spacecraft-to-instrument rotation matrix

### 6.3 Independent Analysis

In addition to the primary pointing analysis completed by KinetX Aerospace, an independent verification and validation (IV&V) team from NASA’s Goddard Space Flight Center (GSFC) developed their own NavCam 1 and 2 pointing solutions by using a different tool on the same star images. The GSFC team processed these images using GIANT (Wright et al. 2018) and followed the following steps to estimate the spacecraft body frame to camera frame alignment for both NavCam 1 and 2:

1. Generate an accurate camera model using star images to map vectors in the camera frame into locations on an image plane.
2. Match the observed star locations from the image with stars in the UCAC4 catalogue.
3. Convert the observed star locations in the image to star directions in the camera frame using the inverse camera model.
4. Perform a static or temperature dependent alignment.

The static-alignment was performed by:

1. Rotating the star directions in the inertial frame taken from the star catalogue into the spacecraft body frame using the post-fit attitude solution for the spacecraft body frame.
2. Estimating the static rotation from the spacecraft body frame to the camera frame by solving Wahba’s problem (Wahba 1965) using Davenport’s Q-Method (Davenport 1968) with the catalogue unit vectors expressed in the spacecraft body frame and the observed unit vectors expressed in the camera frame.

The temperature-dependent alignment was performed by:

1. Using the paired observed and catalogue star directions to solve for the camera frame attitude with respect to the inertial frame using Davenport’s Q-Method solution (Davenport 1968) to Wahba’s problem (Wahba 1965).
2. Find the rotation from the spacecraft body frame to the solved-for camera frame for each image using the post-fit spacecraft body frame attitude.
3. Convert the solved for camera frame rotations from the spacecraft body frame into roll, pitch, and yaw angles.
4. Perform a linear least-squares fit of the form

$$\begin{bmatrix} 1 & T_1 \\ 1 & T_2 \\ \vdots & \vdots \\ 1 & T_n \end{bmatrix} \begin{bmatrix} r_c & p_c & y_c \\ r_l & p_l & y_l \end{bmatrix} = \begin{bmatrix} \tilde{r}_1 & \tilde{p}_1 & \tilde{y}_1 \\ \tilde{r}_2 & \tilde{p}_2 & \tilde{y}_2 \\ \vdots & \vdots & \vdots \\ \tilde{r}_n & \tilde{p}_n & \tilde{y}_n \end{bmatrix} \tag{5}$$

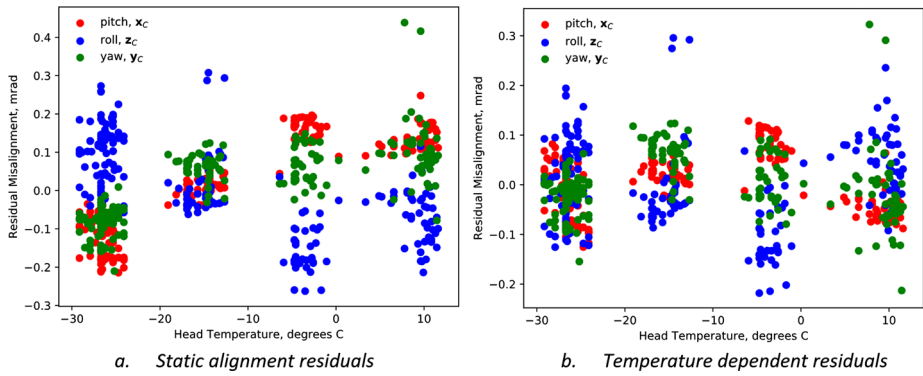


**Fig. 11** Alignment residuals calculated by the GSFC IV&V team for NavCam 1 with (right) and without (left) temperature effects removed

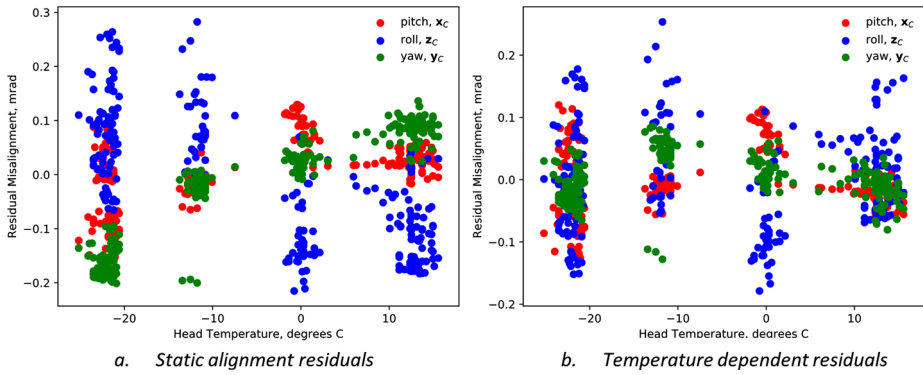


**Fig. 12** Alignment residuals calculated by the GSFC IV&V team for NavCam 2 with (right) and without (left) temperature effects removed

**Table 2** The static and temperature-dependent alignment values for NavCam 1 and 2 calculated by the GSFC IV&V team. These values assume a rotation order of xyz, such that the full rotation is given by  $\mathbf{R}_{cam}^{SC} = \mathbf{R}_z(r) \mathbf{R}_y(y) \mathbf{R}_x(p)$  where  $\mathbf{R}_{cam}^{SC}$  is the rotation from the spacecraft body frame to the camera frame and  $\mathbf{R}_j(\alpha)$  is a rotation of  $\alpha$  about the  $j$  axis

		NavCam 1			NavCam 2		
		$r$	$p$	$y$	$r$	$p$	$y$
Temp.	Constant ( $^{\circ}$ )	69.857	0.0903	-5.980	72.6570	0.0198	14.0862
Dep.	Linear ( $^{\circ}/^{\circ}\text{C}$ )	$3.127\text{e-}4$	$-1.385\text{e-}4$	$-5.363\text{e-}4$	$3.232\text{e-}4$	$-2.984\text{e-}4$	$-2.177\text{e-}4$
Static	Constant ( $^{\circ}$ )	69.853	0.0918	-5.973	72.6570	0.0218	14.0879

where  $T_i$  refers to the  $i$ th camera head temperatures,  $\tilde{r}_i, \tilde{p}_i, \tilde{y}_i$  refer to the measured roll, pitch, and yaw angles from the spacecraft body frame to the camera frame for the  $i$ th image,  $r_c, p_c, y_c$  refer to the constant roll, pitch, and yaw angles from the spacecraft body frame to the camera frame, and  $r_l, p_l, y_l$  refer to the temperature roll, pitch, and yaw coefficients from the spacecraft body frame to the camera frame.

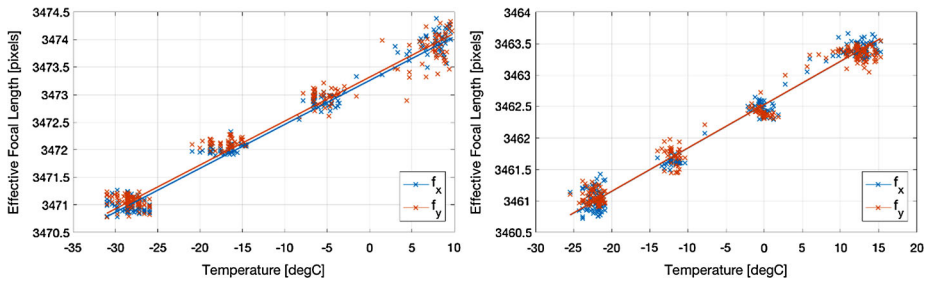


**Fig. 13** NavCam 1 (left) and 2 (right) focal length change with temperature. The change in focal length over the operational temperature range is about 0.1%. To convert the focal length in pixel units to focal length in millimeters multiply by the detector pixel pitch ( $2.2 \times 10^{-3}$  mm)

Table 2 provides the static and temperature dependent alignment values for NavCam 1 and NavCam 2. Figures 11 and 12 show the post-fit residuals for both the static and temperature dependent alignments for NavCam 1 and 2, respectively. There is only a minor temperature dependence in the alignment, which is in agreement with the primary analysis.

## 7 Image Geometry Calibration

### 7.1 Focal Length Calibration Overview

Camera-level thermal vacuum testing performed by the TAGCAMS manufacturer in June 2015 predicted that the effective focal length (EFL) of each TAGCAMS imager would vary slightly over its operational temperature range, approximately  $0.25 \mu\text{m}/^\circ\text{C}$  for NavCam 1 and  $0.18 \mu\text{m}/^\circ\text{C}$  for NavCam 2. To better assess this in-flight, we used the outbound cruise star field images to characterize the effective focal length over the asteroid operations temperature range.

### 7.2 Primary Focal Length Analysis

We calculated the change in focal length by minimizing the cataloged star center residuals in a least-squares sense to estimate three parameters:  $f_{x0}$ ,  $f_{y0}$  (the camera’s focal length in pixels at  $0^\circ\text{C}$  in image space along the long and short axes of the TAGCAMS detector, respectively) and  $a_1$  (the linear slope of the effective focal length change with temperature). These parameters are used to calculate the effective focal lengths,  $f_x$  and  $f_y$ , at any given temperature using the equation:

$$\begin{bmatrix} f_x \\ f_y \end{bmatrix} = \begin{bmatrix} f_{x0} + f_{x0}a_1T \\ f_{y0} + f_{y0}a_1T \end{bmatrix} \tag{6}$$

where  $T$  is the camera head temperature in degrees Celsius. Table 3 shows the best-fit parameter values.

In addition to this batch estimation of the effective focal length’s temperature dependence, we also estimated the focal length separately for each image. These results are plotted together in Fig. 13, where the solid lines indicate the linear function described by Eq. (6)

**Table 3** Focal length fit parameters to Eq. (6), as determined by the primary (KinetX) and IV&V (GSFC) teams

	NavCam 1	NavCam 2
$a_1$ (1/°C) KinetX	2.2933e-5	1.9876e-5
$a_1$ (1/°C) GSFC	2.3744e-5	1.9675e-5

above and the individual data points are the focal lengths estimated separately for each image. This in-flight calibration confirmed that there is a small temperature dependence in the effective focal lengths of both NavCam 1 and 2 of approximately  $0.2 \mu\text{m}/^\circ\text{C}$ .

We encountered difficulties acquiring usable NavCam 1 data at the hot end of the operational temperature spectrum due in part to its mounting angle on the spacecraft instrument deck. As described in Sect. 2, we used the Sun to warm the cameras in a manner analogous to how they are heated during asteroid operations. To achieve the highest operational temperature expected we had to illuminate the spacecraft deck at an angle of  $45^\circ$ . The NavCam 1 boresight is angled  $6^\circ$  away from the normal to the spacecraft deck which brought the solar illumination vector to within  $39^\circ$  of the NavCam 1 boresight in the hot illumination configuration. As described by Bos et al. (2018) we implemented this NavCam 1 pointing offset to simplify the planning and execution of OpNav images while in orbit but this geometry generated a substantial amount of scattered light during the hot calibration activities for NavCam 1. The stray light was so pronounced that every image taken during NavCam 1's first hot calibration campaign was completely saturated and unusable for distortion and focal length calibration. For the second hot calibration campaign, the exposure time was reduced from 10 seconds to 1.6 seconds. This resulted in an image that was partially saturated but still contained some usable data. We used approximately 8 to 10 stars from each of those images, compared to at least 50 stars from images without stray light.

Because of NavCam 2's different pointing configuration, it did not have the same issues as NavCam 1 with acquiring calibration data at hot temperatures. For NavCam 2 we were able to acquire images during its hot calibrations using 10 s exposures with a manageable amount of stray light.

### 7.3 Independent Focal Length Analysis

Similar to the pointing calibration case, the OSIRIS-REx project tasked the IV&V team to complete an independent focal length analysis using the same in-flight dataset analyzed by the KinetX Aerospace team. To perform the focal length analysis the GSFC team completed the following steps:

1. Match the observed star locations from the image with stars in the UCAC4 catalogue.
2. Use the paired observed and catalogue star directions to solve for the camera frame attitude with respect to the inertial frame using Davenport's Q-Method solution (Davenport 1968) to Wahba's problem (Wahba 1965).
3. Rotate the catalogue star directions into the camera frame using the solved for attitude.
4. Use the current estimate of the camera model to project the catalog unit vectors onto the image.
5. Update the camera model to minimize the residuals between the projected and extracted stars in a least squares sense for all images.

We used the Brown camera model (Brown 1966), with a linear temperature dependence on the focal length and a residual pointing misalignment term included for each image. This is given by

$$\mathbf{x}'_C = \mathbf{R}_{\delta\theta} \mathbf{x}_C$$

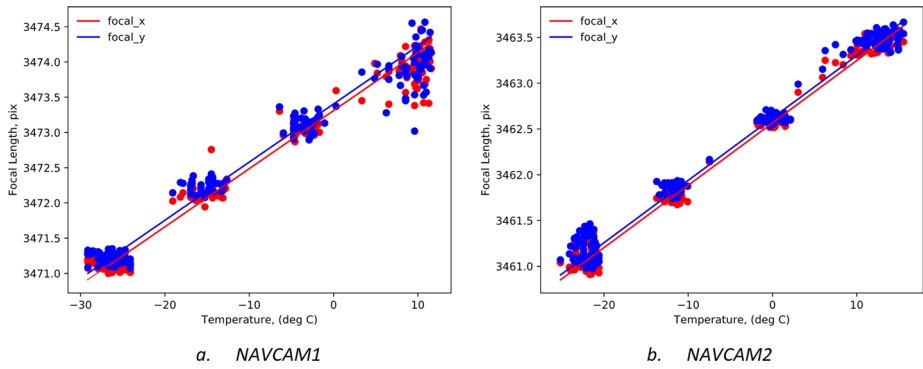


**Fig. 14** NavCam 1 (left) and 2 (right) focal length change with temperature calculated by the GSFC IV&V team. Similar to the results shown in Fig. 13, the change in focal length over the operational temperature range is about 0.1%. To convert the focal length in pixel units to focal length in millimeters multiply by the detector pixel pitch ( $2.2 \times 10^{-3}$  mm)

$$\begin{aligned}
 \mathbf{x}_I &= \frac{1}{z'_c} \begin{bmatrix} x'_c \\ y'_c \end{bmatrix}, r = \sqrt{\mathbf{x}'_I \mathbf{x}_I} \\
 \mathbf{x}'_I &= (1 + k_1 r^2 + k_2 r^4 + k_3 r^6) \mathbf{x}_I + \begin{bmatrix} 2p_1 x_I y_I + p_2 (r^2 + 2x_I^2) \\ p_1 (r^2 + 2y_I^2) + 2p_2 x_I y_I \end{bmatrix} \\
 \mathbf{x}_p &= \begin{bmatrix} f_x & 0 & c_x \\ 0 & f_y & c_y \end{bmatrix} \begin{bmatrix} (1 + a_1 T) \mathbf{x}'_I \\ 1 \end{bmatrix} \tag{7}
 \end{aligned}$$

where  $\mathbf{x}_C = [x_C \ y_C \ z_C]^T$  is a vector in the camera frame,  $\mathbf{R}_{\delta\theta}$  is a residual misalignment rotation matrix,  $k_{1-3}$  are radial distortion coefficients,  $p_{1-2}$  are tangential distortion coefficients,  $T$  is the camera head temperature in degrees Celsius,  $a_1$  is the linear temperature dependence constant,  $f_x$  and  $f_y$  are the  $x$  and  $y$  focal lengths expressed in units of pixels, and  $c_x$  and  $c_y$  are the location of the principal point (the location where the axis of zero distortion pierces the image plane) expressed in units of pixels.

Table 3 shows the results for the linear temperature dependence coefficients for NavCam 1 and 2. In addition, to check the temperature dependence, we estimated the  $x$  and  $y$  focal lengths (the focal lengths along the long and short axes of the detector, respectively) individually for each image. Figure 14 shows the individual focal lengths for each image in units of pixels, as well as the temperature-dependent focal length fit. The linear fit accurately models the focal length as a function of temperature. In addition, the estimated focal length temperature coefficients compare well with the KinetX results.

### 7.4 Optical Distortion Calibration Overview

The final component required to accurately map object space to the cameras' detector planes is calibration of the cameras' optical distortion. Both NavCam 1 and 2 nominally have 13.9% of barrel distortion at the corners of their fields of view, which, if left uncorrected would cause an offset error of 225 pixels (63 mrad). The camera vendor completed a pre-launch optical distortion calibration campaign but we obtained better information using the same in-flight star field images used to calibrate camera pointing and focal length.



## 7.5 Primary Optical Distortion Calibration

For the primary optical distortion calibration of NavCam 1 and 2 we used the OpenCV distortion model (OpenCV 2014). This model uses nine parameters: three parameters to model radial distortion  $k_1$ ,  $k_2$  and  $k_3$ ; two parameters to model tangential distortion  $p_1$  and  $p_2$ ; two parameters to describe the intersection point of the optical axis with the image plane  $c_x$  and  $c_y$ ; the effective focal lengths along the long and short axes of the detector array  $f_x$  and  $f_y$ , respectively, which are both dependent on the camera temperature as described in the previous section. The algebraic formulation of the OpenCV model used for this calibration is as follows:

$$\begin{aligned} \begin{bmatrix} x' \\ y' \end{bmatrix} &= \frac{1}{z} \begin{bmatrix} x \\ y \end{bmatrix} \\ r^2 &= x'^2 + y'^2 \\ \begin{bmatrix} x'' \\ y'' \end{bmatrix} &= (1 + k_1 r^2 + k_2 r^4 + k_3 r^6) \begin{bmatrix} x' \\ y' \end{bmatrix} + \begin{bmatrix} 2p_1 x' y' + p_2 (r^2 + 2x'^2) \\ p_1 (r^2 + 2y'^2) + 2p_2 x' y' \end{bmatrix} \\ \begin{bmatrix} u \\ v \end{bmatrix} &= \begin{bmatrix} f_x & 0 \\ 0 & f_y \end{bmatrix} \begin{bmatrix} x'' \\ y'' \\ 1 \end{bmatrix}. \end{aligned} \quad (8)$$

We find a unit vector  $[x, y, z]$  describing a star's position for each cataloged star using its inertial position as defined by the UCAC4 star catalog rotated into the instrument frame using the camera attitude. We then normalize this unit vector by its Z-component and apply the distortion model shown above. The resulting unit-less coordinates  $x''$ ,  $y''$  are converted to pixels by multiplying by the effective focal length for each dimension. These coordinates are with respect to the optical axis intersection point, so they need to be added to the coordinates of the optical axis intersection point to determine the star's location in image coordinates  $(u, v)$ . The star center residual error is then the difference between this predicted star location and the observed star location in the image.

We implemented a Levenberg-Marquardt least squares algorithm to estimate these distortion parameters as well as to re-estimate the camera attitude for each image so that the star center residuals were minimized in a global sense. The criteria for an ideal distortion calibration result is two-fold. First, the residuals should show a zero-mean Gaussian distribution with a standard deviation less than the expected center finding in both image dimensions ( $\sim 0.1$  pixels for NavCam 1 and 2). Second, the residuals should point in random directions across the FOV, showing no systematic structure related to the stars' positions in the image.

Both NavCam 1 and 2 exhibited a relatively large amount of distortion due to their wide field of view. This can be clearly seen in the star center residuals shown in Fig. 15 when no distortion model is used. There is obvious strong radial distortion, especially at the edges and corners of the FOV. The length of each error vector is equal to the magnitude of the residuals, which are larger than 150 pixels at the corners.

After calibration, the star center residuals become much smaller and the radial pattern disappears. Figure 16 shows the post-calibration star center residuals at each star's location in the image. Some slight "banding" is observed in these plots. This is due to bright stars moving across the field of view as the spacecraft rolls between each calibration image to observe a new point in space while maintaining a constant solar illumination vector on the spacecraft. In these plots, we magnified the length of the vectors by a factor of 200 so that

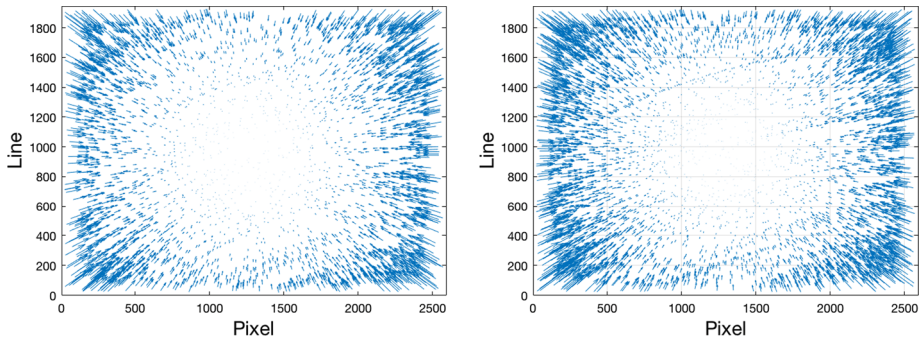


**Fig. 15** NavCam 1 (left) and 2 (right) pre-calibration star center error vectors illustrating the differences between the predicted star locations and the actual star locations indicated by the tip of the arrows. The vector lengths are actual size. The vectors located near the corners span more than 150 pixels

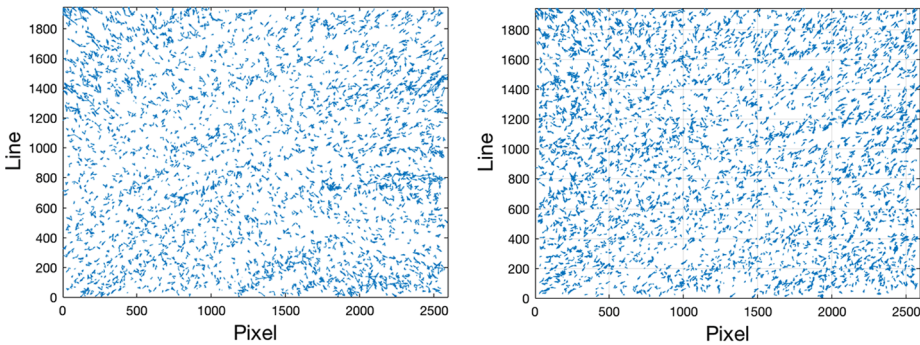


**Fig. 16** NavCam 1 (left) and 2 (right) post-calibration star center error vectors illustrating the differences between the predicted star locations and the actual star locations. The vector lengths shown are magnified by 200 times so that they are visible. The random nature of the vector directions indicates that the distortion fits are free of bias

they are visible. The vectors mostly point in random directions throughout the field of view showing that the remaining error is random and not due to incorrect or biased modeling of the optical distortion, which would show structure in the residual vectors similar to Fig. 15. Star center-finding error and star catalog position error from the UCAC4 catalog contribute to the remaining error. Figure 17 shows that the post-fit residual error in both cameras is less than 0.1 pixel,  $1-\sigma$ . The final distortion parameter fit values are summarized in Table 4.

### 7.6 Independent Optical Distortion Calibration

The GSFC IV&V team independently calibrated the optical distortion in NavCam 1 and 2 using in-flight star images. The calibration used the same steps followed to estimate the focal length temperature described in Sect. 7.3 above. We performed a least-squares fit using a Levenberg-Marquardt algorithm as described by Christian et al. (2016). In the fit, the parameters  $[f_x \ f_y \ k_1 \ k_2 \ k_3 \ p_1 \ p_2 \ a_1 \ c_x \ c_y \ \delta\theta_1 \ \dots \ \delta\theta_n]$  were estimated based on the residuals of all images where  $\delta\theta_i$  is a three-element rotation vector for the  $i$ th image.

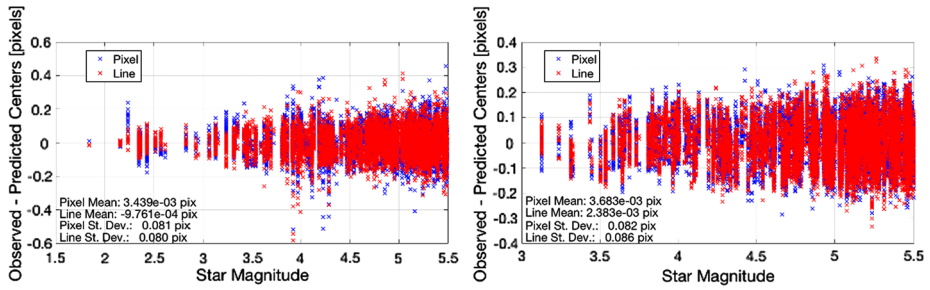


**Fig. 17** NavCam 1 (left) and 2 (right) post-calibration star center error versus stellar magnitude. For both cameras the 1- $\sigma$  error is less than 0.1 pixels

**Table 4** Optical distortion fit parameters for the primary (KinetX) and IV&V (GSFC) calibration efforts for NavCam 1 and 2. The focal lengths,  $f_{x0}$  and  $f_{y0}$ , are the calculated focal lengths at 0 °C

Parameter	NavCam 1 KinetX	NavCam 1 GSFC	NavCam 2 KinetX	NavCam 2 GSFC
$k_1$	-0.53766	-0.539	-0.53831	-0.539
$k_2$	0.37526	0.388	0.38214	0.389
$k_3$	-0.18368	-0.214	-0.20281	-0.218
$p_1$	2.3432e-4	-2.56e-4	-6.2239e-4	-1.30e-4
$p_2$	9.0875e-4	8.64e-4	-1.2388e-4	2.04e-5
$f_{x0}$ (pixels)	3473.260	3473.3	3462.530	3462.6
$f_{y0}$ (pixels)	3473.321	3473.4	3462.532	3462.6
$c_x$	1269.083	1269.7 <sup>a</sup>	1310.530	1310.4 <sup>a</sup>
$c_y$	950.747	950.6 <sup>a</sup>	969.487	968.9 <sup>a</sup>
$a_1$	2.2933e-5	2.3744e-5	1.9876e-5	2.0400e-5

<sup>a</sup>The GSFC optical distortion model’s coordinate system uses a (0, 0) origin, while the KinetX origin is (1, 1) based. For direct comparison between the GSFC and KinetX results we have added 1 to the GSFC  $C_x$  and  $C_y$  values

Traditionally, misalignment and the camera principal point cannot be simultaneously estimated. This is because the misalignment and principal points are highly correlated (to first order they both appear as a linear bias). For NavCam 1 and 2, however, we found that it was necessary to simultaneously estimate these parameters due to the significant distortion. In our case we found the misalignment and the principal point simultaneously observable due to: the large amount of distortion, the wide field of view and the large number of images included in the fit.

The resulting camera model for each camera (minus the misalignment terms) is given in Table 4. The distortion maps are shown in Fig. 18 and the post-fit residuals are presented in Figs. 19, 20, and 21. The post-fit standard deviation of the residuals is approximately 0.1 pixels and the overall residual directions and magnitudes appear mostly random, with no readily observable bias. In addition, the results show good agreement with the primary calibration parameters calculated by KinetX Aerospace.

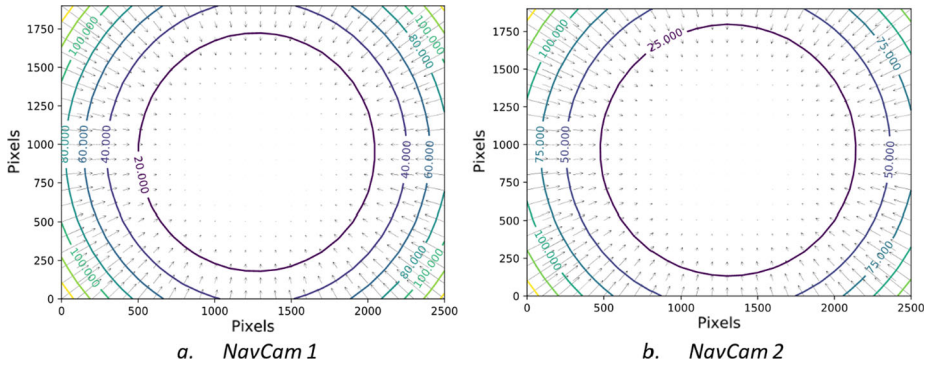
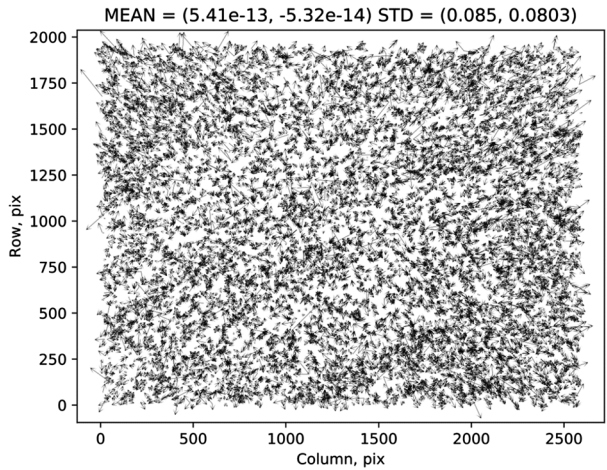
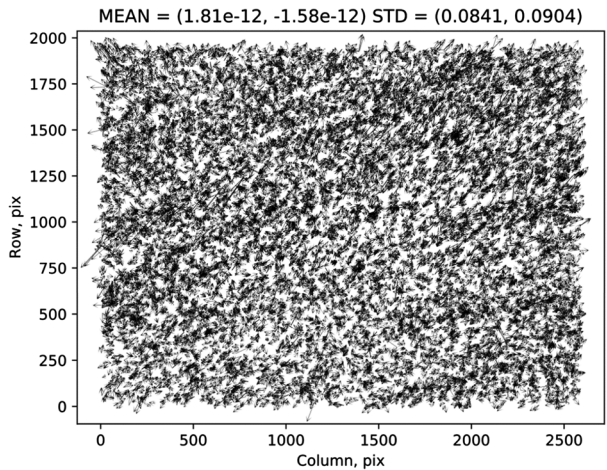


**Fig. 18** NavCam 1 (left) and 2 (right) optical distortion contour maps produced by the GSFC IV&V team. The contour lines indicate the amount of positional error in pixels

**Fig. 19** NavCam 1 (top) and 2 (bottom) quiver plots showing the post-distortion fit residual errors. The random nature of the vector directions indicates the distortion fits are free of bias



*a. NavCam 1*



*b. NavCam 2*

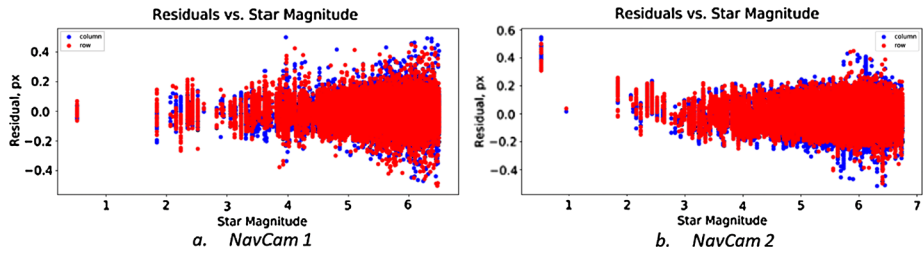


**Fig. 20** NavCam 1 (left) and 2 (right) post-calibration star center error versus stellar magnitude calculated by the GSFC IV&V team. For both cameras the  $1\text{-}\sigma$  error is less than 0.1 pixels. The GSFC IV&V analyses used a broader range of star magnitudes than those used in the KinetX analyses. These plots cover a larger range of stellar magnitude than those shown in Fig. 17

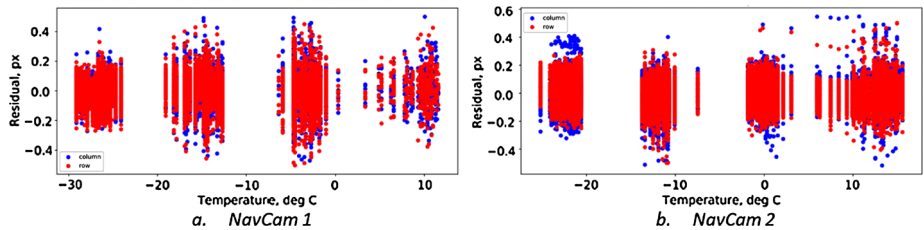


**Fig. 21** NavCam 1 (left) and 2 (right) post-calibration star center error versus temperature calculated by the GSFC IV&V team. The results indicate that after the focal length change with temperature is taken into account, the residual error is independent of temperature

## 8 Image Quality Characterization

### 8.1 Point Spread Function (PSF) and Modulation Transfer Function (MTF) Estimation

To support our asteroid image analysis and processing efforts, we analyzed a portion of the outbound cruise calibration dataset to assess the post-launch PSF and camera resolution. We initially analyzed 291 observations of the bright star Fomalhaut from the Launch +6 Month calibration campaign and 174 observations of Pollux from the Launch +18 Month calibration campaign. Each of these data sets positioned the target star in 13 different locations across the NavCam 1 and 2 fields of view (Fig. 22).

We first processed the images by using the dark reference pixel region to subtract the DN offset and mean dark current from the pixels in the active portion of the array. To calculate a PSF with a better signal-to-noise ratio than possible in a single frame we combined two star images, a 0.5-s exposure and a 5-s exposure, to produce hybrid PSFs. The 5-s exposure saturated the core of the PSFs but provided information on the PSF periphery. The 0.5-s exposure provided unsaturated information on the PSF core. When the observations were planned we expected that the spacecraft pointing drift between the acquisition of the two exposures would be small enough that we would be able to extract the core pixel values from the 0.5-s exposure images to replace the saturated pixel values in the 5-s exposure images at the same pixel coordinates. However, we discovered that enough of a sub-pixel change in pointing occurred between the image acquisitions to introduce discontinuities into the PSF slopes.



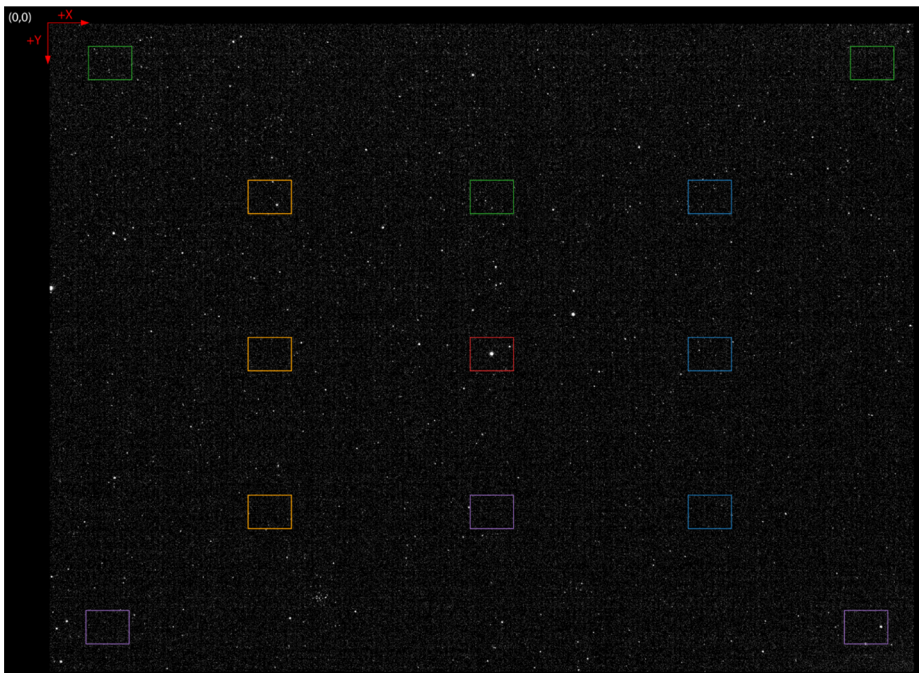


**Fig. 22** Example of a star-field image used to assess NavCam 1 and 2 PSF and image quality. The zones highlighted by colored rectangles indicate the 13 different positions where the bright target star (either Fomalhaut or Pollux) would be located with different spacecraft attitudes. In this case, the target star is located at the center of the field of view inside the red rectangle. The image orientation is the same as shown in Fig. 6

To work around the issue of the shifting PSFs we implemented a five-step correction process to remove the PSF discontinuities:

1. Normalize PSF by exposure time.
2. Compute the shift between the images using cross-correlation.
3. Up-sample the 0.5-s image from  $10 \times 10$  pixels to  $1000 \times 1000$  pixels using bi-cubic interpolation with a spline representation of the ideal-sampling sinc function.
4. Shift the 0.5-s up-sampled sub-frame by the shift computed in Step 2.
5. Down-sample the shifted 0.5-s sub-frame back to  $10 \times 10$  pixels using bi-cubic interpolation.
6. Replace every saturated pixel value in the 5-s image with the resampled 0.5 s sub-frame values at the same pixel location.

Step 3 is sensitive to noise, so we inspected every interpolated sub-frame to identify obvious non-physical results. We found that for a few images there was either too much noise or too much stray light in the background to produce reliable results. In those instances we removed the PSFs from further consideration.

Visual inspection of the hybrid PSFs showed small variations across the fields of view of both NavCam 1 and 2 with generally the best imaging performance (i.e. smaller PSFs and better resolution) generally occurring near the centers of the fields of view. This behavior agrees with the performance predicted from the design-residual aberrations of the NavCam lens design prescription. We also found qualitatively that the PSFs did not substantially change between the Launch +6 Month and Launch +18 Month calibration campaigns. We

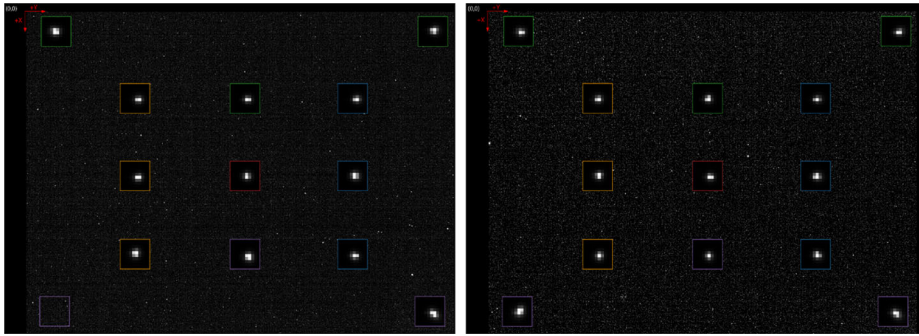


**Fig. 23** NavCam 1 hybrid PSFs constructed from 0.5-s and 5-s exposure images. Results from the Launch +6 Month and +18 Month calibration campaigns are shown on the left and right, respectively. The PSFs shown are enlarged  $20\times$  with respect to the rest of the image and located in the positions from which they were calculated. The Launch +6 Month PSF in the lower left corner was omitted because of a questionable result caused by stray light. The results indicate similar performance throughout most of the field of view and similar performance over time

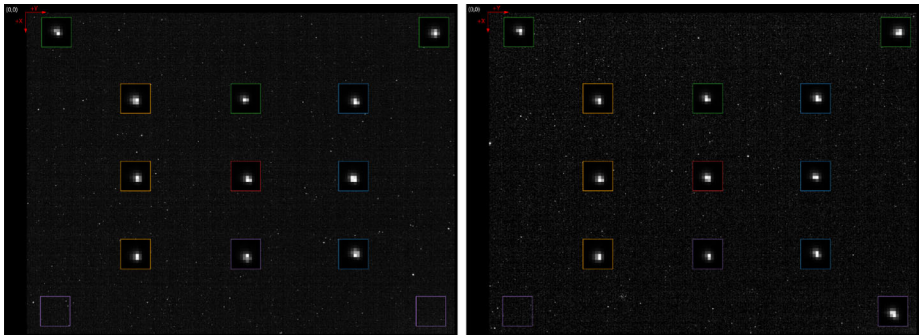


**Fig. 24** NavCam 2 hybrid PSFs constructed from 0.5-s and 5-s exposure images. Results from the Launch +6 Month and +18 Month calibration campaigns are shown on the left and right, respectively. The PSFs shown are enlarged  $20\times$  with respect to the rest of the image and located in the positions from which they were calculated. PSFs with questionable features due to stray light were omitted. The results indicate similar performance throughout most of the field of view and similar performance over time

attribute variations that are visible to differing optical PSF registrations with respect to the detector array. Figures 23 and 24 show the hybrid PSFs for NavCam 1 and 2, respectively.

To assess the image quality changes in a more quantitative fashion we calculated horizontal and vertical modulation transfer function (MTF) profiles from the hybrid PSFs using the FFT (Fast Fourier Transform). Figure 25 shows the results for NavCam 1 for the Launch +6 Month and Launch +18 Month calibration campaigns. Figure 26 shows the results for NavCam 2 for the Launch +6 Month and Launch +18 Month calibration campaigns.

During the TAGCAMS ground test we found the MTF measurements to vary significantly depending on the target and laboratory illumination conditions. The ground test did not measure MTF directly, instead, we used the camera response to edge targets to estimate MTF values at various spatial frequencies. This measurement approach is known to have considerable difficulties that depend on the quality of the target (particularly with respect to the target black-level radiance) and the uniformity of the target irradiance. However, us-



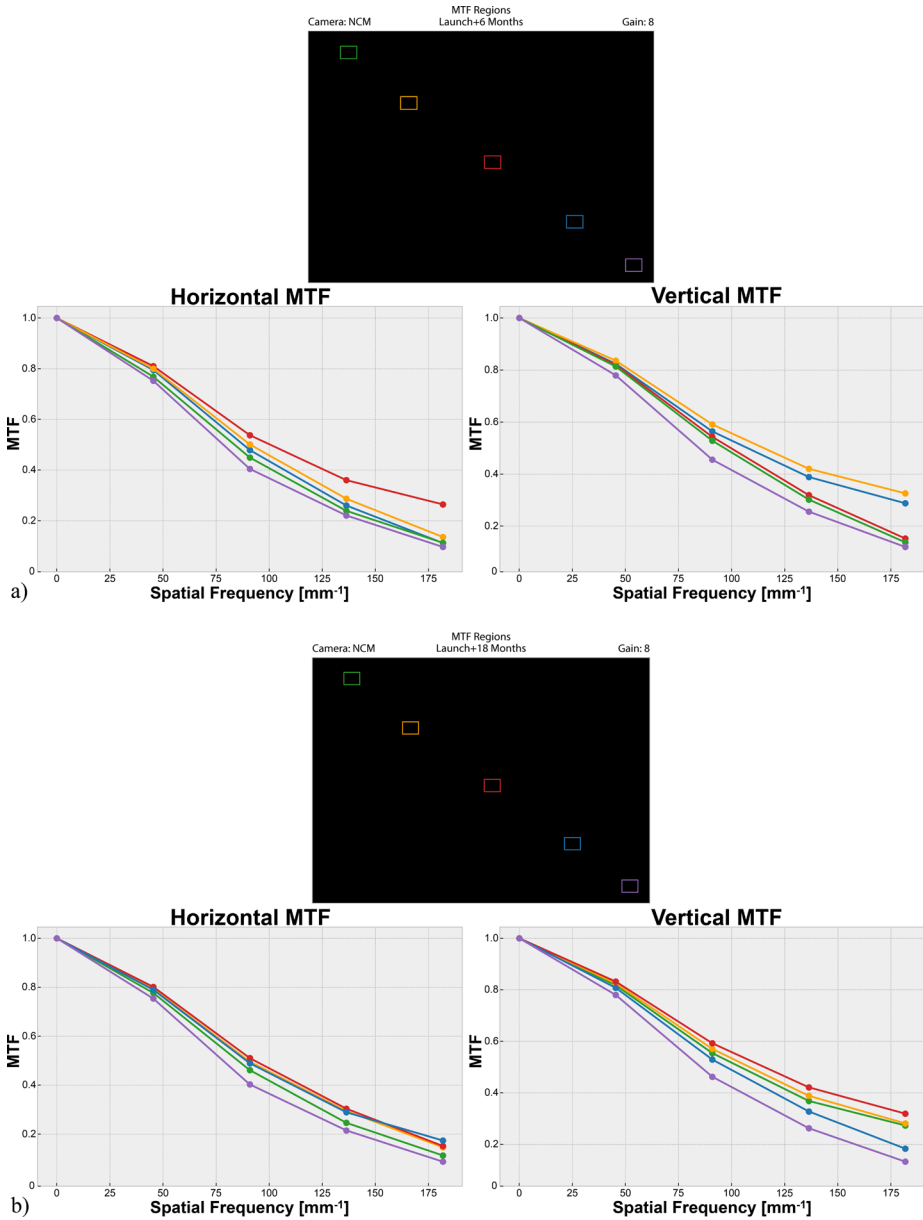


**Fig. 25** NavCam 1 horizontal and vertical MTF results calculated from the hybrid PSFs from the Launch +6 Month (a) and Launch +18 Month (b). The MTF profile line colors correspond to the locations shown in the camera’s field of view directly above the plots. Although the resolution at the center of the field of view is generally better than the resolution at the corners, we attribute most of the spread in the MTF results to the variability in how well the target star was centered on a detector pixel in a given exposure

ing this approach, we found the TAGCAMS MTF, near the center of the fields of view, to be approximately 0.36 at the cold operational temperature at a mid-spatial frequency of  $130 \text{ mm}^{-1}$ . This was slightly less than the MTF predicted for the system. Polychromatic

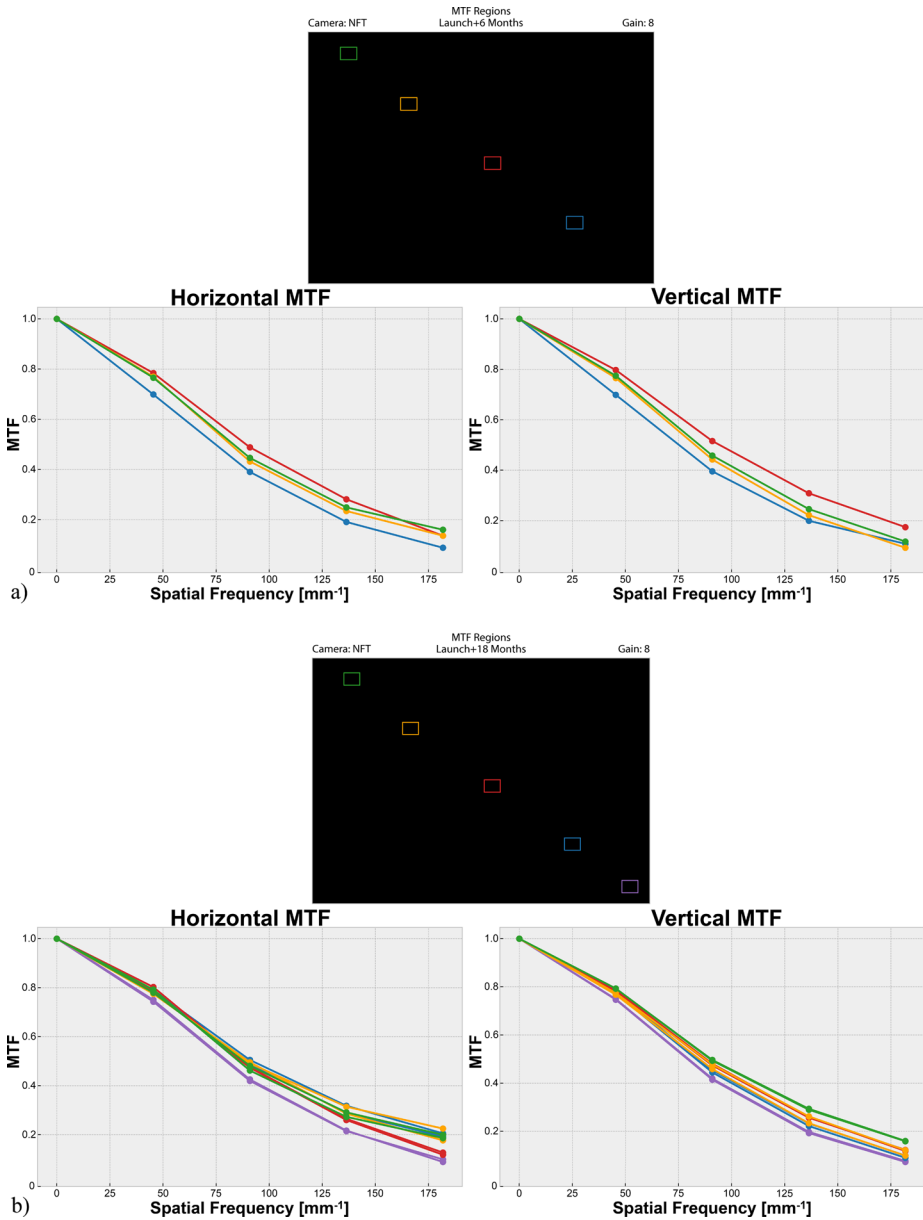


**Fig. 26** NavCam 2 horizontal and vertical MTF results calculated from the hybrid PSFs from the Launch +6 Month (a) and Launch +18 Month (b) calibration datasets. The MTF profile line colors correspond to the locations shown in the camera’s field of view directly above the plots. Although the resolution at the center of the field of view is generally better than the resolution at the corners, most of the spread in the MTF results we attribute to the variability in how well the target star was centered on a detector pixel in a given exposure

MTF calculations using the lens design prescription multiplied by the pixel MTF indicated that the system (without construction, alignment and environmental errors) would have an MTF at 130 mm<sup>-1</sup> of 0.47-0.51 (depending on what value is used for the pixel effective

width). In addition, some of the worst-case results for NavCam 2 suggest that its MTF performance is the worst of the three cameras, perhaps as low as  $0.29$  at  $130 \text{ mm}^{-1}$ . But the differences are also at the same level as the measurement noise. Nevertheless, the level of performance estimates were consistent with the specifications and deemed acceptable before launch.

Our NavCam 1 in-flight MTF analysis showed performance ranging from  $0.20$  to  $0.40$  across the field of view at a spatial frequency of  $130 \text{ mm}^{-1}$  for the Launch +6 Month dataset and  $0.20$  to  $0.38$  across the field of view for the Launch +18 Month dataset. For NavCam 2 the values ranged from  $0.19$  to  $0.31$  for the Launch +6 Month dataset and  $0.20$  to  $0.31$  for the Launch +18 Month dataset at the same  $130 \text{ mm}^{-1}$  spatial frequency. These in-flight results are in agreement with what we measured during the ground test campaign, indicating that the resolution of the two cameras is comparable to the ground test measurements and did not change substantively over the 18 months the cameras were in space. The results also indicate that the resolution is best near the centers of the NavCam 1 and 2 fields of view. Finally, the in-flight results indicate that the NavCam 1 resolution is slightly better than NavCam 2's, consistent with the ground test results.

## 8.2 Point Spread Function (PSF) Estimation Across the Field of View

In addition to the PSF and MTF estimates that we produced using Fomalhaut and Pollux, we also took advantage of observations of other, dimmer stars to estimate PSF morphology across NavCam 1's field of view. For typical NavCam 1 long exposures (exposure times  $>2$  s), good signal-to-noise ratio ( $>20$ ) observations of stars as dim as 6th apparent magnitude can be acquired. This provides a much higher sampling of the camera field of view than the 13 locations tested as described in the previous section.

To take advantage of the additional stellar observations, we divided the  $2592 \times 1944$  active area of the NavCam 1 images into a  $9 \times 5$  grid of isoplanatic, equally-spaced regions where we assumed that the spatially-variant PSF was effectively constant. We selected the size of the grid by balancing the goal of making the regions as small as possible while keeping them large enough to sample a sufficient number of stars to reconstruct the PSF.

After applying image corrections for the DN offset and mean dark current, we up-sampled by a factor of eight every catalogued star within each isoplanatic region using a bi-cubic spline representation of the sinc function. From inspection, a factor of eight up-sampling appeared to be the resampling limit before the images of dimmer stars started to show sampling artifacts due to image noise. We then normalized the intensity values of the resampled images using their apparent magnitudes.

Next, the processing calculated a center position for each star using a moments-based formulation with an adaptive threshold. To test the centroiding accuracy we ran Monte Carlo analyses using synthetic star images with known centroids and found the maximum error to be  $< 1/10$  of a NavCam 1 pixel. We then used the centroids to position each up-sampled and normalized star image of an isoplanatic region into a common coordinate system. The processing then added the image of each star within a region on a pixel-by-pixel basis to synthesize a high-resolution PSF representation at each of the 45 regions in the NavCam 1 field of view.

Figure 27 shows the results of the processing applied to a NavCam 1 20-s exposure acquired just after launch during the Launch +14 Day checkout. The resampled PSFs show similar behavior to the PSFs acquired using the technique described in the previous section. The PSFs in the central portion of the NavCam 1 field of view have the narrowest widths where the camera offers the highest resolution. The PSF grows in size with radial distance

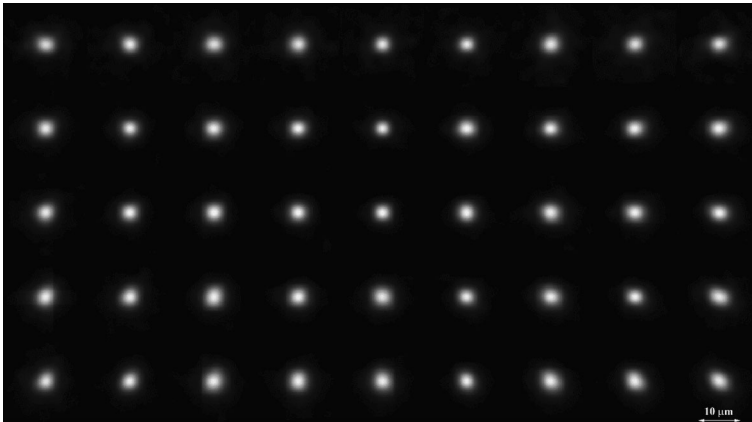


**Fig. 27** NavCam 1 high-resolution PSF estimates across the field of view from star observations acquired with a 20 s exposure during the Launch +14 Day checkout activity. Each estimate was created by normalizing and stacking the images of multiple stars within a sub-window of the image. The orientation and parity of the figure matches what is shown in Fig. 6. A 10- $\mu\text{m}$  scale bar is shown in the lower right corner

from the field of view center and becomes best-sampled at the corners of the field of view. Comparing Fig. 27 to Fig. 23 shows the same pronounced astigmatic shape of the PSF at the lowest right corner of the field of view whereas the upper right corner of the field of view shows a large PSF with a less pronounced astigmatic shape.

## 9 Stray Light Observations

### 9.1 Out-of-Field Stray Light

During the TAGCAMS development phase, the mission operations plan prescribed a minimum boresight-to-Sun angle of  $80^\circ$  for NavCam1 and 2. The TAGCAMS developers used this angle to verify the worst-case out-of-field stray light performance of the cameras through a combination of non-sequential ray trace modeling and laboratory “sanity checks”. At the end of the TAGCAMS development, the OSIRIS-REx project determined that NavCam 1 would need to provide optical navigation images of Bennu with the Sun approximately  $45^\circ$  off of the camera’s boresight during two fly-bys during the Detailed Survey phase of the mission (Lauretta et al. 2017). Subsequent stray light analyses using a non-sequential ray trace model of the camera and spacecraft nadir deck indicated that the additional stray light caused by the almost 50% reduction in boresight-to-Sun angle would be insignificant, less than the detector noise during the observation and at least a factor of ten below the observation requirement.

On April 16, 2017, we acquired 39 NavCam 1 calibration images using 10-s exposures as part of the Launch +6 Month Calibration Part 1 campaign. The purpose of these observations was to calibrate camera pointing and optical distortion when the Sun heats up the TAGCAMS and the spacecraft nadir deck to the maximum temperature expected during asteroid operations (approximately  $10^\circ\text{C}$ ). The solar illumination geometry during these observations closely matched the expected high-phase-angle Detailed Survey geometry and created a Sun-to-boresight angle for NavCam 1 of  $39^\circ$ . All 39 NavCam 1 images acquired with this illumination geometry were saturated due to stray light. Similar NavCam 1 imaging during

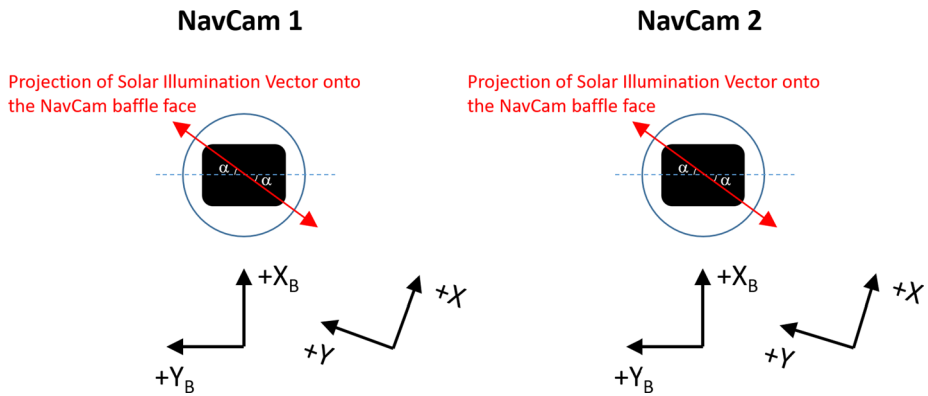


**Fig. 28** Illustration of the NavCam 1 and 2 baffle illumination geometries used during the SOSC scattered light scans with the EM NavCam.  $X_B$  and  $Y_B$  are local baffle coordinates.  $X$  and  $Y$  are spacecraft coordinates (the slight spacecraft  $Z$  component in the plane is not shown). Both coordinate system origins are shown offset from their actual positions for clarity. Simulated solar irradiance at 1 AU was scanned across the baffle face at three  $\alpha$  angles ( $0^\circ$ ,  $37^\circ$  and  $90^\circ$ ). For the same Sun-to-boresight angle, the testing indicated the scattered light was greatest with  $\alpha = 37^\circ$ , the least with  $\alpha = 90^\circ$  and intermediate with  $\alpha = 0^\circ$

the Launch +6 Month Calibration Part 2 campaign with a slightly larger Sun-to-boresight angle of  $49^\circ$  and a shorter exposure time of 4 s, produced images with substantial stray light signatures as well. The images were not saturated, but large portions of the corners of the field of view were dominated by stray light.

Following these observations we used the non-sequential ray-trace model of NavCam 1 and the spacecraft nadir deck to explore the cause of the stray light observations. The investigation indicated that the stray light was caused by direct solar illumination of the interior of the NavCam 1 baffle, which scattered light to other baffle and lens surfaces until finally striking the detector. Although the ray-trace modeling provided insight into the stray light mechanism, even by incorporating new, worst-case assumptions for surface properties, we were unable to predict the same intensity level of scattered light on the detector as captured in the in-flight images. Undoubtedly some feature (likely an edge radius or surface property) was built into the camera baffles that was not included in the design information from which the stray light model was constructed.

Because the scattered light modeling could not reproduce the signal levels seen in the actual data, we initiated a new ground test using the engineering model (EM) NavCam still on the ground along with a solar simulator and dark room at the Lockheed Martin Space Operations Simulation Center (SOSC) (Milenkovich and D'Souza 2012). We illuminated the EM NavCam with simulated sunlight at various Sun-to-boresight angles while acquiring long-exposure images that maximized the signal-to-noise ratio of the scattered light measurement. Figure 28 illustrates the three different illumination scan angles,  $\alpha$  ( $0^\circ$ ,  $37^\circ$  and  $90^\circ$ ), that were tested with both the NavCam 1 and 2 geometries. In addition, three specific geometries were tested at compound illumination angles that matched in-flight calibration illumination conditions with Sun-to-boresight angles of:  $39^\circ$ ,  $49^\circ$  and  $59^\circ$ . Figure 29 shows the compound angles that produced the  $39^\circ$  Sun-to-boresight angle on April 16, 2017, and resulted in 39 saturated NavCam 1 images.

Reduction of the SOSC stray light scan data indicated that the NavCam 1 and 2 are most susceptible to generating scattered light when  $\alpha = 37^\circ$ . This is understandable because the margin between the camera field of view and the baffle edges is smallest in the extreme

## NavCam Illumination Geometry

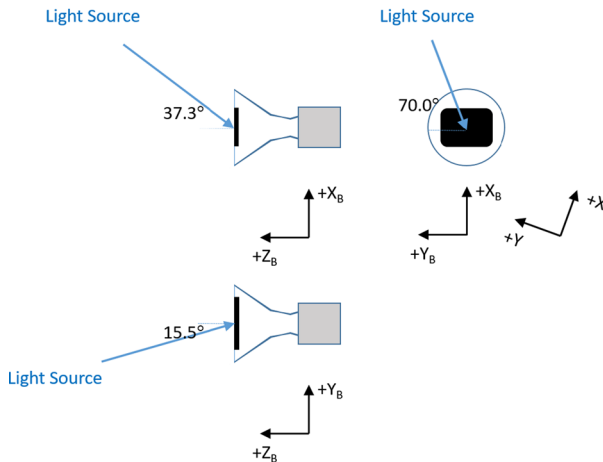


**Fig. 29** Illustration of the NavCam baffle illumination for one of the three specific solar illumination geometries explored during the SOSC scattered light test with the EM NavCam, using the same coordinate system shown in Fig. 28. The angles  $37.3^\circ$ ,  $15.5^\circ$  and  $70.0^\circ$  correspond to the NavCam 1 solar illumination geometry encountered during the Launch +6 Month Calibration Part 1 campaign that set up a  $39^\circ$  Sun-to-boresight angle and produced 39 saturated images with 10-s exposures. Configurations with angles of  $57.9^\circ$ ,  $26.2^\circ$  and  $72.9^\circ$  (corresponding to a Sun-to-boresight angle of  $49^\circ$ ) and  $47.3^\circ$ ,  $21.5^\circ$  and  $70.0^\circ$  (corresponding to a sun-to-boresight angle of  $59^\circ$ ) were also tested on the EM NavCam for comparison with other in-flight data

corners due to the large amount of optical distortion. The least susceptible geometry to stray light is when  $\alpha = 90^\circ$ . We observe intermediate performance when  $\alpha = 0^\circ$ . In addition, we found that the specific NavCam 1 illumination geometry of April 16, 2017, produced a scattered light signal with peaks in the corners of the field of view that ranged from 3,000 to 5,000 DN/s when operating in 12-bit mode with a gain setting of 1.0 for an equivalent heliocentric distance of 1 AU. The scattered light signal over most of the field of view and at the center was 1,000 DN/s for this condition. Thus, even though the OSIRIS-REx spacecraft heliocentric distance was 1.17 AU on April 16, 2017, the images were still overexposed by about a factor of two.

We used the SOSC ground test measurements during the planning stages of the Launch +18 Month Calibration campaign to ensure that we could acquire unsaturated NavCam 1 star-field images to test camera pointing and optical distortion stability at the highest temperature predicted for asteroid operations. We chose an exposure time of 1.6 s (instead of 10 s) with a gain setting of 1.0. This exposure was long enough to reliably detect stars but short enough to keep the scattered light from saturating the entire field of view.

Figure 30 shows a NavCam 1 image example from the Launch +18 Month Calibration campaign when the Sun-to-boresight angle was  $39^\circ$  and the exposure time was set to 1.6 s. Unlike the images from the Launch +6 Month Calibration Part 1 campaign with the identical illumination conditions, only a portion of the field of view in the Launch +18 Month data was unusable due to saturation and the image coordinate transformation calibration could be checked using stars as described in Sect. 7.

As Fig. 30 shows, the agreement between the scattered light features in the in-flight data and the EM NavCam images was very good. We understand the phenomena well enough to choose exposure times during the Detailed Survey fly-bys with high phase angles. The



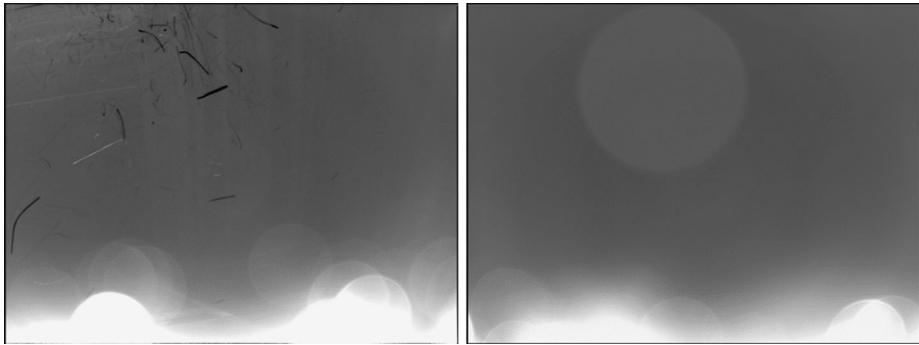


**Fig. 30** EM NavCam image acquired during the SOSC scattered light ground test with a Sun-to-boresight angle of  $39^\circ$  (left). NavCam 1 image acquired during the Launch +18 Month Calibration campaign with the same illumination geometry (right). The dark and bright linear features in the left, middle-left and upper-left portions of the EM NavCam image are laboratory artifacts. The circular features in both images are due to light scattering from particulates located on the first lens surface. In both images, the light is coming from the upper left portion of the field of view at an angle of  $70^\circ$  relative to the horizontal and illuminates the interior of the baffle closest to the bottom of the field of view, with the peak near the lower right corner. The excellent correlation in stray light performance between the two cameras demonstrates that the EM ground test results are suitable for planning high-phase-angle observations of Bennu. The image format in this figure is flipped  $180^\circ$  about a vertical axis from the diagram shown in Fig. 6

SOSC testing indicates that the scattered light signal is non-linear with angle and depends on the projected angle of the sunlight with respect to the camera baffle face. For the same Sun-to-boresight angle, sunlight produces roughly 10 times more scattered light when the solar vector projection is along the baffle face diagonal ( $\alpha = 37^\circ$  in Fig. 28) as to when it is orientated vertically ( $\alpha = 90^\circ$  in Fig. 28). We did not take suitable data, either in-flight or on the ground, to develop an accurate parametric model that depends on angle to predict how much of the stray light that scatters off the baffle-interior will illuminate the detector. In place of such a model we primarily rely on the results of the three specific cases measured on the ground and in-flight when the Sun-to-boresight angles were  $39^\circ$ ,  $49^\circ$  and  $59^\circ$  to set imaging parameters, with the heaviest emphasis on the  $39^\circ$  case. Current operations planning indicates that NavCam 1 and 2 imaging geometries will not be more challenging than the  $39^\circ$  Sun-to-boresight angle case shown in Fig. 29. The worst-case estimate based on this geometry is that when observations prescribe Sun-to-boresight angles below  $60^\circ$ , stray light will be present at a rate not exceeding 1,000 DN/s over most of the field of view (12-bit mode, gain of 1.0).

## 9.2 In-Field Stray Light

Unlike out-of-field scattered light, we expected early in the TAGCAMS development phase that in-flight scattered light was a performance parameter that we would need to monitor closely for most imaging conditions. As described by Bos et al. (2018), half of the optical navigation images planned for the NavCams use long exposures ( $\geq 2$  s) to image star fields while Bennu is wholly contained within the camera's field of view. These long exposures oversaturate the portions of the image containing Bennu by 400 to 500 times, depending on albedo and topography. Because of these considerations, we spent considerable resources on the camera baffle design and specified high-performance, low-reflectivity coatings for the lens surfaces.

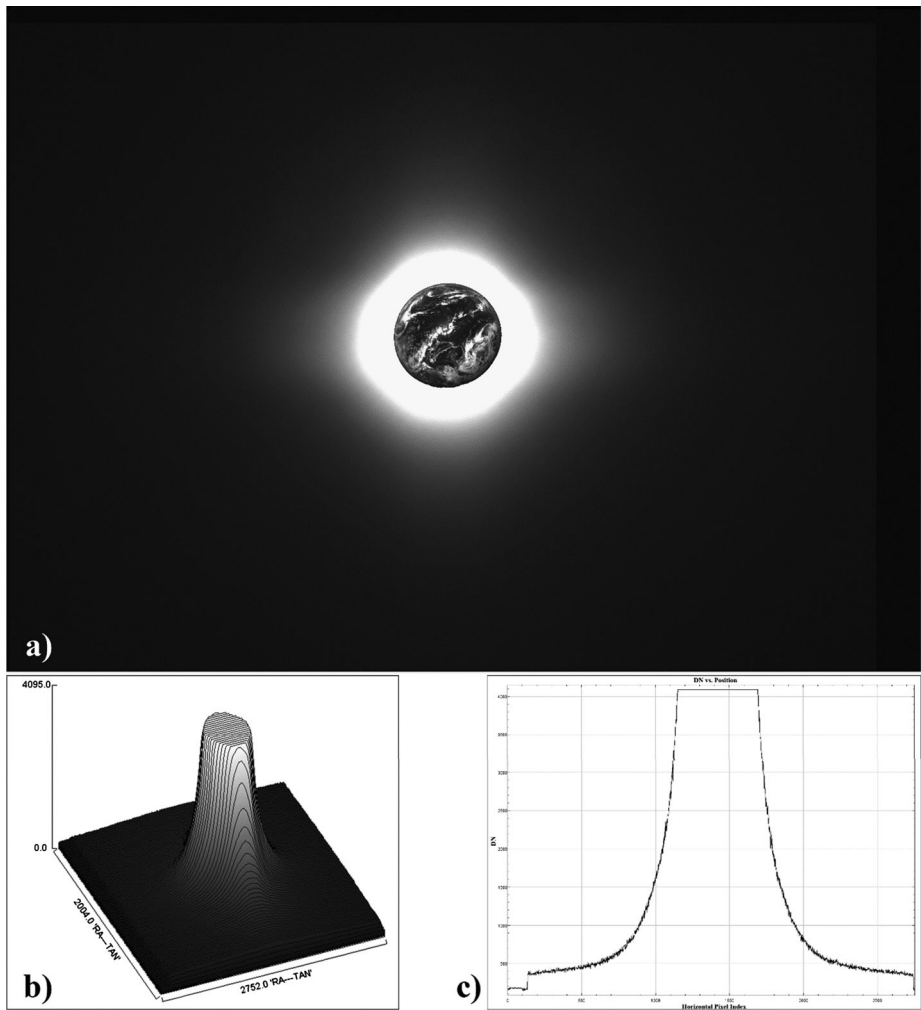


**Fig. 31** Example of the NavCam 1 in-flight scattered light control from the OSIRIS-REx Earth fly-by. The top image (a) is a composite image of a properly exposed 0.0764-ms Earth image overlaid on a 0.4-s over-exposed image acquired 15 s later on September 22, 2017. The 0.4 s image is over-exposed by a factor of 1,510, but most of the image area provides sufficient dynamic range for imaging stars. The lower left figure (b) is a contour map of the over-exposed image. The lower right plot (c) shows a horizontal profile through the center of the saturated area of the over-exposed image

Although TAGCAMS in-field scattered light performance was tested on the ground, both in the laboratory with the flight units and under the night sky with the EM NavCam (Bos et al. 2018), we took advantage of the Earth fly-by opportunity and acquired over-exposed images of Earth to check performance in-flight. Testing stray light performance over such a large dynamic range is challenging in the laboratory due to the difficulty with controlling reflections from laboratory components, so we expected the in-flight performance assessment to improve considerably from what we observed pre-launch.

Figure 31 shows an example of the most over-exposed image that we took of Earth during the fly-by, a 0.4-s long exposure with NavCam 1. The 0.4-s image was over-exposed by a

factor of 1,510. Even though the Earth disk and a portion of the field of view around it are saturated, there are large portions of the field of view where substantial dynamic range remains to image stars. This was considerably better performance than what we were able to verify on the ground. Based on this result, we may increase the planned exposure times of our long optical navigation images of Bennu from 2 s to 5 s in order to detect dimmer objects.

### 9.3 StowCam Observations

Of the 1,183 TAGCAMS images we acquired during the outbound cruise, only 81 were StowCam images. For the nine discrete imaging campaigns described in Sect. 2, we acquired StowCam images during each of them except during the OCAMS Stray Light Ride-Along on January 18, 2018.

Unlike the NavCam 1 and 2 imaging campaigns, whose primary purpose was the cross-check and improvement of the ground-based calibration and characterization, the primary purpose of the StowCam outbound cruise imaging was to monitor the camera's performance and document the spacecraft deck conditions. StowCam's pointing is fixed on the spacecraft deck to view the SRC and document the asteroid sample stowage. The SRC dominates the StowCam's field of view and only small portions of deep space in the upper right and left corners of the image are visible. Pursuing imaging campaigns to generate in-flight StowCam calibration products would be impractical and unnecessary given mission goals. The most important quantitative result from the StowCam imaging was confirmation of the suitability of the selected exposure times given various spacecraft illumination conditions.

During the first four imaging campaigns, we acquired five StowCam images at each opportunity using the same five exposure times (0.005, 0.01, 0.02, 0.03, and 0.04 s). For the Launch +14 Day Checkout we used the same image settings we ran during OSIRIS-REx spacecraft ground processing to check instrument health. At the Launch +6 Month Calibration Part 1 opportunity we used the same exposure times but modified some of the camera settings to check the performance of various compression and image sub-framing operations. Then starting with the Launch +6 Month Calibration Part 2 campaign we reverted back to using the same image settings on the first five images and added an additional six images to the standard imaging set to bring the total number to eleven. The additional exposures increased the range of exposure times for the set such that any spacecraft deck illumination would produce at least one image with a high signal-to-noise ratio without saturating. We continued to run this eleven-image set throughout the rest of the outbound cruise phase. During the Launch +18 Month Calibration campaign we took the eleven image set twice to check performance with two different spacecraft deck illumination geometries.

Figure 32 shows examples of the StowCam images acquired during the Launch +14 Day, +10 Month Checkout, +18 Month and the Launch +22 Month checkouts. These particular images we acquired using a 0.04 s exposure time, a gain of 1.25 and JPEG compression. In the figure, the image intensity is scaled identically in all four images. The overall image brightness differences are primarily due to different heliocentric spacecraft distances. The primary spacecraft components visible in the images are the sample return capsule (SRC) in the center of the frame, the SamCam radiator and sunshade in the lower left and the NavCam 1 camera head wrapped in thermal blanketing in the lower right. These images were acquired with an identical solar illumination geometry with the spacecraft +X axis pointed at the Sun so that most of the nadir deck was in the shadow cast by the high-gain antenna. Almost all of the illumination seen in the images in Fig. 32 was caused by the scattering of light off of a small number of surfaces that were directly illuminated by the sun. The intensity level

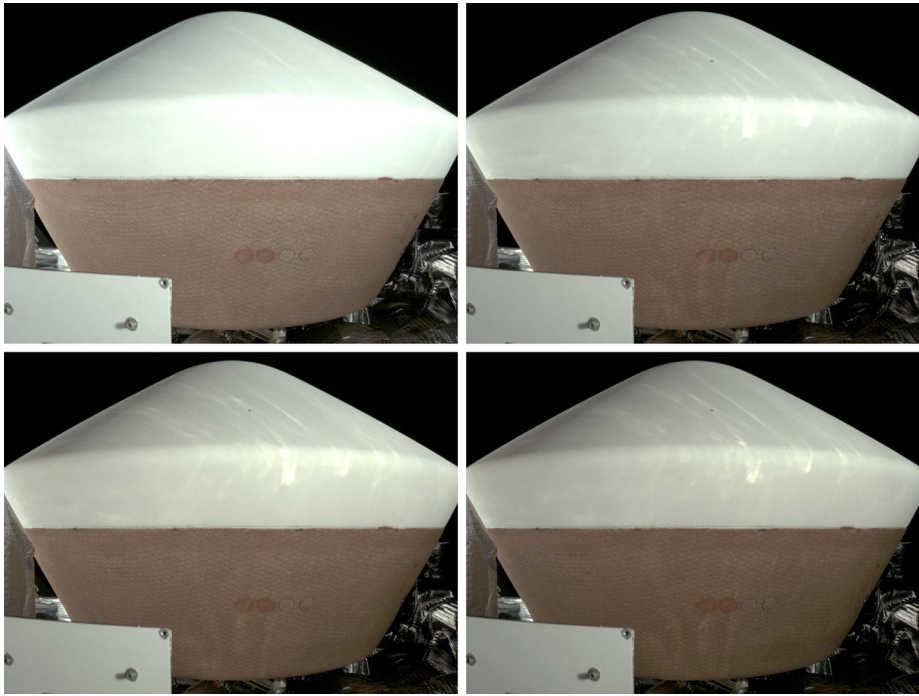
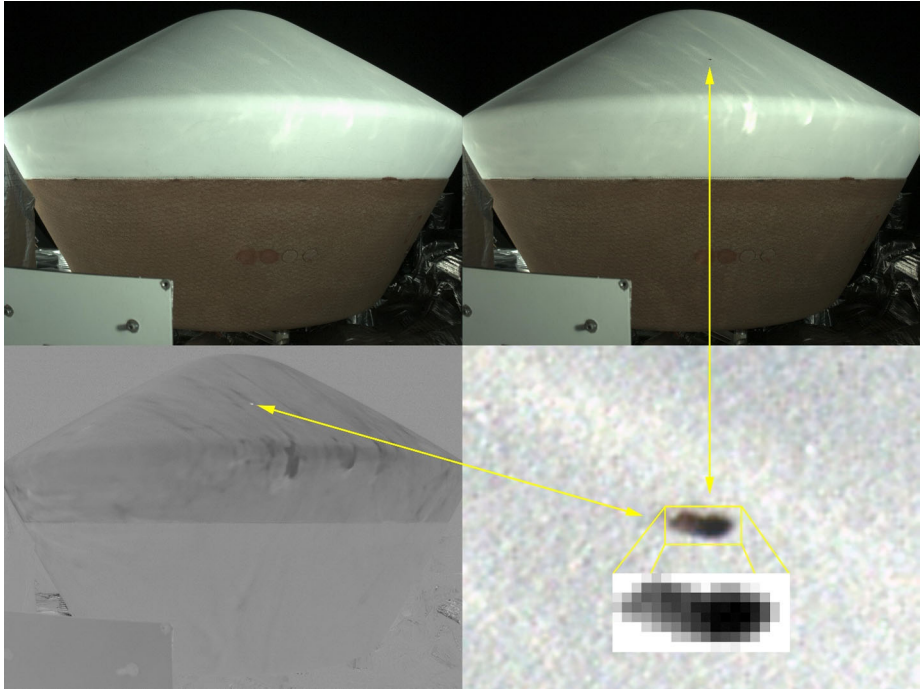


**Fig. 32** Example of the StowCam images acquired during the Launch +14 Day Checkout (September 22, 2016; upper left), the Launch +10 Month Checkout (August 3, 2017; upper right), the Launch +18 Month Checkout (March 12, 2018; lower left) and the Launch +22 Month Checkout (July 22, 2018; lower right). These images were all acquired using a 0.04-s exposure time, a gain of 1.25 and JPEG compression. The image intensity is scaled identically in all four images. The overall image brightness differences are primarily due to different heliocentric spacecraft distances. The greenish tint in the upper left image is due to the large number of green pixels that are saturated in the image. The primary spacecraft components visible in the images are the sample return capsule (SRC), the SamCam radiator and sunshade (lower left) and the NavCam 1 camera head wrapped in thermal blanketing (lower right). Direct sunlight is coming from the left side of the images but most of the illumination is due to the scattering of direct sunlight from spacecraft surfaces (primarily from the OSIRIS-REx Thermal Emission Spectrometer and the PolyCam) that are not in the field of view. This is the reason for the bolt head shadow on the SamCam radiator pointing to the left

and general uniformity of the scattered light was better than anticipated and has caused us to re-examine how we will illuminate the spacecraft deck during the asteroid sample stow operation.

In early 2017, the spacecraft navigation team detected evidence that the OSIRIS-REx trajectory was being slightly affected by spacecraft outgassing. In an effort to check on the status of the spacecraft deck, we ran the five-image StowCam sequence on March 2, 2017. The StowCam imagery did not reveal any outgassing activity or significant changes to the spacecraft deck but we did detect a small change in the SRC heatshield.

Figure 33 compares the 0.04-s StowCam exposures from the Launch +14 Day Checkout and the StowCam Spacecraft Outgas Monitoring activity. After scaling the image intensity by heliocentric distance, we subtracted the two images from each other to create a difference image. Most of the differences we detected in the differenced image were due to changes in illumination caused by small changes in the temperature-dependent thermal blanketing surface shapes but one physical change was confirmed in the SRC heatshield. In the later



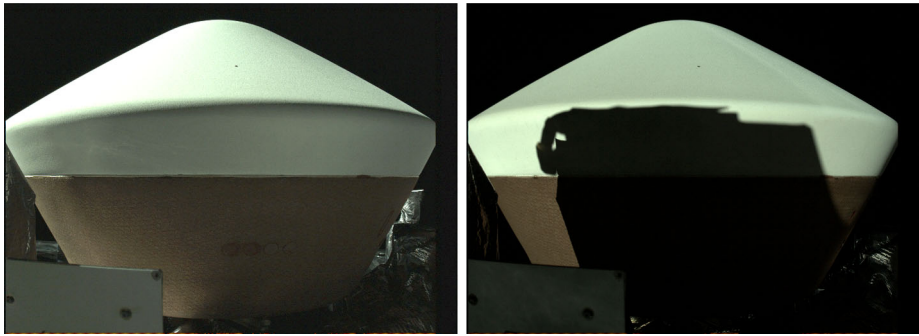
**Fig. 33** A comparison of 0.04-s StowCam exposures from the Launch +14 Day Checkout (September 22, 2016; upper left) and the StowCam Spacecraft Outgas Monitoring activity (March 2, 2017; upper right). After scaling the image intensity by heliocentric distance, the two top images were subtracted to create the difference image in the lower left. Most of the differences observed are due to changes in illumination caused by small changes in the temperature-sensitive thermal blanketing surface radii but one physical change was evident in the SRC heatshield. This change is magnified and shown with a DN histogram stretch in the lower right

image we observed a small feature on the upper portion of the heatshield that was not present in the earlier image. The feature was either a divot in the ablative heatshield material or a contaminate with a dark albedo attached to the heatshield.

Subsequent ray trace modeling using non-sequential optical models for the StowCam and the spacecraft nadir deck indicated that the feature's width was 1.5 to 2.5 mm. We determined this by reverse tracing rays from the StowCam detector plane through the StowCam optics until they intersected the SRC. The ray intercept coordinates provided an estimate for the feature's size.

Three months after the feature's discovery we determined definitively that the new SRC feature was a 1.5 to 2.5 mm divot and not a piece of contamination after we acquired new StowCam images using direct instead of indirect solar illumination on June 12, 2017. Direct solar illumination of the SRC feature did not create a corresponding shadow on the SRC and made part of the feature darker than previously observed due to the geometry of the orientation. This feature was most likely caused by a micrometeoroid strike of the SRC sometime after 17:23 UTC on September 22, 2016, but before 14:52 UTC on March 2, 2017. The spacecraft team performed an assessment of the minor change to the SRC heatshield and found that the 2 mm-wide depression would not affect the SRC's performance upon reentry. The heatshield is ablative by design and much larger portions of it will ablate after it enters Earth's upper atmosphere during the sample return.





**Fig. 34** Two StowCam images of the OSIRIS-REx spacecraft deck acquired under direct sunlight. The image on the left is an 8-bit, uncompressed 0.3228-ms exposure with a gain of 1.0 acquired on June 12, 2017, at a heliocentric distance of 1.27 AU as part of the Launch +6 Month Calibration Part 2 activities. In this image the sunlight is coming in from the upper left part of the frame and illuminates the spacecraft deck at an angle of incidence of  $55^\circ$ . The direct sunlight falling on NavCam 1 in the lower right part of the frame makes it highly visible. A small portion of the NavCam 1 white baffle face is visible. The image on the right is an 8-bit, uncompressed 0.3228 ms exposure with a gain of 1.0 acquired on March 8, 2018 at a heliocentric distance of 1.13 AU as part of the Launch +18 Month Calibration activities. In this image direct sunlight is coming in from the left hand side of the image  $30^\circ$  off the boresight of StowCam. The large shadow on the SRC is from the student experiment REXIS (Regolith X-Ray Imaging Spectrometer) located on the spacecraft deck

In addition to the typical StowCam images we commanded when most of the spacecraft deck was in the shadow of the high-gain antenna (i.e. the spacecraft +X axis pointed at the sun), as discussed earlier we also acquired images with the SRC in direct sunlight. We did this on two occasions: June 12, 2017, as part of the Launch +6 Month Calibration Part 2 activity and on March 8, 2018, as part of the Launch +18 Month Calibration activity. Figure 34 shows how the SRC and its surroundings appear under direct sunlight. The image on the left of Fig. 34 is an 8-bit, uncompressed 0.3228 ms exposure with a gain of 1.0 acquired on June 12, 2017, as part of the Launch +6 Month Calibration Part 2 activities. In this image the sunlight is coming in from the upper left part of the frame and illuminates the spacecraft deck at an angle of incidence of  $55^\circ$ . The direct sunlight falling on NavCam 1 in the lower right part of the frame makes it highly visible. A small sliver of the white NavCam 1 baffle face is visible. The image on the right is an 8-bit, uncompressed 0.3228 ms exposure with a gain of 1.0 acquired on March 8, 2018, as part of the Launch +18 Month Calibration activities. In this image direct sunlight is coming in from the left hand side of the image in the XY plane of the spacecraft,  $30^\circ$  off the boresight of StowCam. The large shadow on the SRC is caused by the student experiment REXIS (Regolith X-Ray Imaging Spectrometer) on the spacecraft deck prior to its cover deployment.

The StowCam images acquired during outbound cruise proved the most useful for checking the pre-launch exposure time calculations for the sample stow documentation. We will use the images acquired with both direct and indirect sunlight to select the optimum exposure times once the final sample stow illumination geometry is selected.

#### 9.4 Spacecraft Particulate Observations

Throughout the OSIRIS-REx outbound cruise period NavCam 1 and 2 captured image anomalies, image features that couldn't be attributed to catalogued stars or known planetary bodies. The majority of the time, image anomalies were rare occurrences and we attributed them to radiation artifacts.



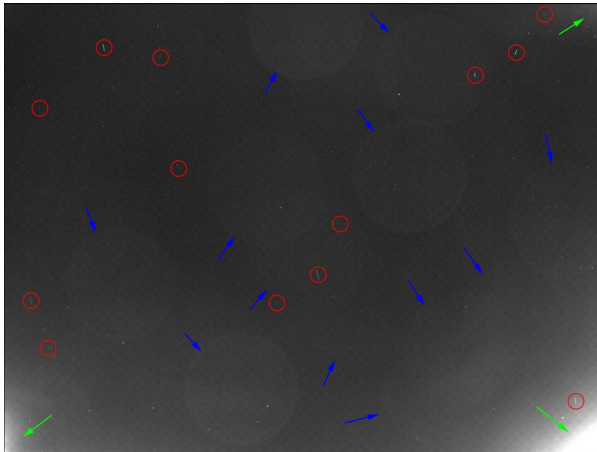


**Fig. 35** NavCam 2 8-bit image acquired on April 10, 2017, using a 5-s exposure and a gain setting of 1.25 which shows three types of image artifacts. The green arrows in the corners point to stray light caused by out-of-field solar illumination coming from the upper left of the image and illuminating the inner baffle surfaces of NavCam 2 (as described in Sect. 9.1). The blue arrows point to stray light artifacts caused by light scatter from particulates located on the first lens surface of NavCam 2. The red circles indicate the new image anomalies observed as streaks in the images. The image format in this figure is flipped 180° about a vertical axis from the diagram shown in Fig. 6

Starting on April 10, 2017, we began detecting image anomalies with a higher frequency and a morphology that we had not previously observed. These anomalies typically appeared as unresolved streaks of varying lengths with uniform intensity. Figure 35 shows an example.

Although our image processing algorithms could ignore the streak anomalies and not jeopardize the goals of the in-flight calibration campaign, we investigated the anomalies further to determine their source. We were motivated by two considerations. First, we wanted to ensure that the anomalies were not artifacts internal to the cameras. Second, we knew that if the spacecraft was generating the anomalies, then the presence of such objects could complicate the search for Bennu natural satellites during asteroid operations as well as other science-related imaging campaigns.

Our initial investigation commenced with a visual inspection of NavCam 1 and 2 image frames. We reviewed images from: April 10, 2017 (58 frames); April 11, 2017 (78 frames); April 13, 2017 (116 frames); April 16, 2017 (78 frames); April 17, 2017 (50 frames); and June 12, 2017 (78 frames). These were observations acquired as part of the Launch +6 Month Calibration Parts 1 and 2 campaigns. All 458 images were visually examined for streaks and we detected a total of 286.

After review of the total set of image streaks, we could not identify any features consistent with internal camera contaminants. Some of the streaks may have been caused by radiation events but some images showed correlation between the features from frame to frame which is not consistent with the transient nature of anomalies caused by cosmic rays or energetic particles. An assessment of the space weather conditions and the behavior of other radiation-sensitive components on the spacecraft also indicated that the environment was similar to the conditions the spacecraft had been experiencing since launch. We concluded that most of the observed streak anomalies were due to real objects located in space in front of and exterior to the cameras.

Unfortunately, due to the large depth-of-field of NavCam 1 and 2 and their focuses set to their hyperfocal distances, we could not definitively determine whether most of the objects

were moving away or moving toward the cameras. For the objects that the cameras captured in a single frame, the change in range was not large enough to use an object's radiometry to determine depth information due to the uncertainty in the point-source photometry caused by the  $< 100\%$  pixel fill-factor discussed in Sect. 3. In most cases our knowledge of the particle motion was constrained to a two-dimensional plane.

One characteristic that we were able to ascertain from the data was that the observation frequency appeared to be related to spacecraft attitude. In particular we noticed that the anomaly activity increased when the solar angle of incidence on the spacecraft deck decreased. Figure 36 plots the number of anomalies observed versus time along with the solar illumination angle of incidence. The correlation between anomaly activity and the solar angle of incidence on the spacecraft nadir deck is strong for the first three days and the fifth day examined (April 10, 11, 13, and 17). This led us to believe that the image anomalies observed were due to the liberation of objects from the spacecraft deck caused by solar illumination and resultant heating.

The correlation of anomaly activity with solar illumination angle of incidence seemed to disappear in the April 16, 2017, and June 12, 2017, results. During the observations made on April 16 and June 12 the angles of incidence were  $45^\circ$  and  $55^\circ$ , respectively, which, based on the data from previous days, should have caused a large amount of activity. We believe these illumination angles did in fact produce activity but by the time of image acquisition the reservoir of objects had been exhausted. As described in Sect. 2, the goal of the observations on those days was to take images after high-temperature thermal equilibrium conditions had been achieved. Before imaging commenced on those days, sunlight had illuminated the spacecraft deck for more than 12 hours. We contend that by the time the imaging commenced the anomalous object population had already been depleted from the reservoir and dissipated from the camera fields of view.

Given the mounting evidence that the bulk of image anomalies were due to objects escaping from the spacecraft deck, we further investigated streak geometry to explore the possible locations of the object reservoirs. First, we examined the few examples where the same object was observed in more than one frame. Figure 37 shows three images acquired by NavCam 2 of the same two anomalous objects. We deduce from the radiometry that the two objects are moving away from the cameras and spacecraft and, based on the streak orientation, the objects are generally moving away from the  $+X$  side of the spacecraft (i.e. away from the high-gain antenna).

To develop statistics on the objects' direction of travel, we analyzed the 286 image streaks and binned the streak angular orientation from  $0^\circ$  to  $180^\circ$  in  $10^\circ$  bins. The  $90^\circ$  orientation in the images is indicated in red in Fig. 37. The histograms for the two most active days of observations are shown in Fig. 38. The data show that the majority of streaks had an orientation of  $90^\circ$  in the images. To determine the plane in which the bulk of objects must be traveling, we used the non-sequential ray trace model of the spacecraft deck and NavCam 1 and 2 to perform reverse ray traces. We traced rays from a series of vertical points in the camera detector planes and used the resulting object-space ray vectors to establish the planes within which the objects were constrained to travel if they produced a  $90^\circ$  streak orientation. Figure 39 shows lines that are contained within those planes (traced from the center of the fields of view) in relation to the spacecraft deck.

The directional analysis led us to believe that the bulk of the anomalous objects were coming from an area on the spacecraft deck in between the SRC (shown in the center of Fig. 39) and the high-gain antenna (the large object on the right side of Fig. 39). We hypothesized that these areas on the spacecraft serve as cold reservoirs where water vapor escaping primarily from the SRC heatshield condenses into ice monolayers that build up over time

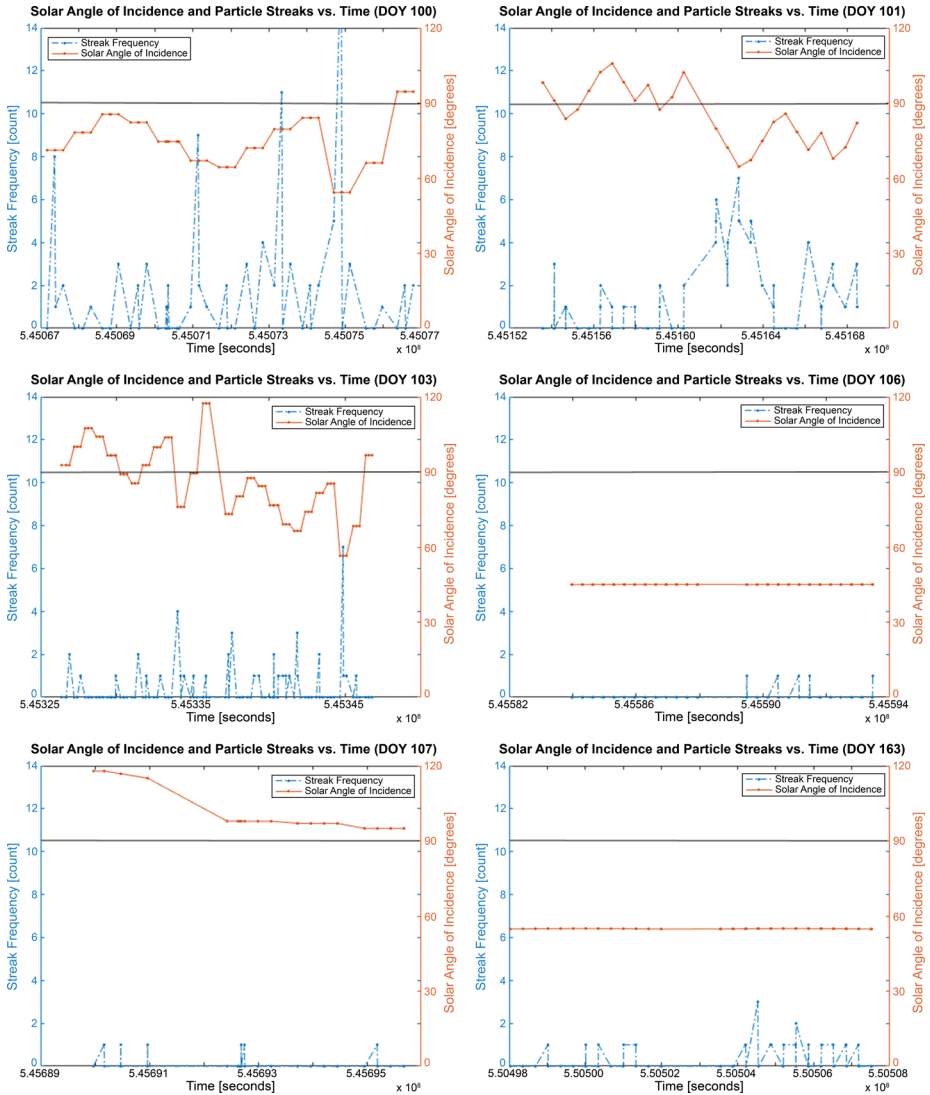


**Fig. 36** NavCam 1 and 2 image anomaly activity versus time (blue) plotted with the spacecraft nadir deck solar angle of incidence versus time (orange). The six days of observations shown are for April 10, 2017 (DOY 100); April 11, 2017 (DOY 101); April 13, 2017 (DOY 103); April 16, 2017 (DOY 106); April 17, 2017 (DOY 107); and June 12, 2017 (DOY 163). The solid black line is a reference to indicate when the Sun went below the spacecraft deck, putting it in shadow. We believe the dearth of activity on DOY 106 and DOY 163 with the low solar angle of incidence is due to the length of time between when the low solar angle of incidence was achieved and imaging commenced (>12 hours)

while most of the spacecraft deck remains shaded by the high-gain antenna. The spacecraft maintained this Sun-point geometry (spacecraft +X-axis pointed at the Sun) throughout most of the time during outbound cruise. When instrument observations called for deviations from this geometry, portions of the spacecraft deck that were freshly illuminated by

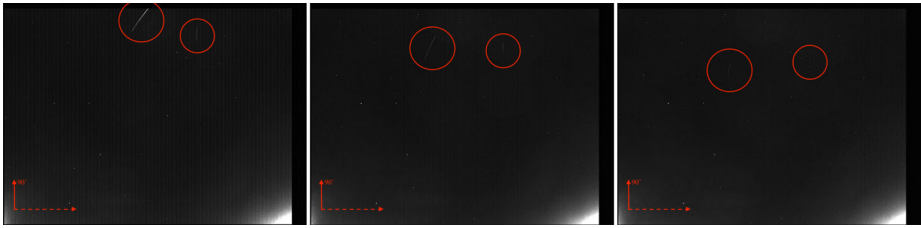


**Fig. 37** Three NavCam 2 image frames showing anomalous object motion from the top of the frame toward the bottom. Assessment of the objects' intensity indicates that they are moving away from NavCam 2 and the spacecraft. The image format in this figure is flipped 180° about a vertical axis from the diagram shown in Fig. 6

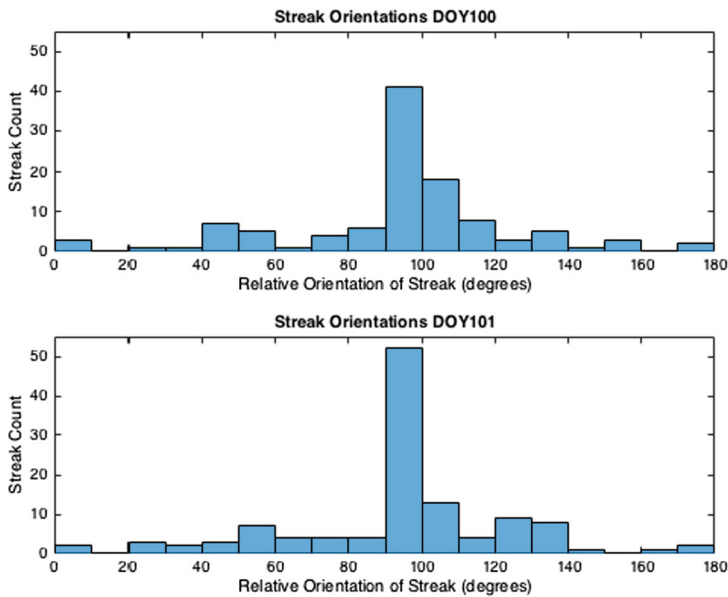


**Fig. 38** Histograms of streak orientations from the two most active days of anomalous object activity. DOY 100 (top) is April 10, 2017. DOY 101 (bottom) is April 11, 2017. The majority of observed streaks had roughly a 90° image orientation (see Fig. 37)

the Sun heated up, causing the sublimation and release of solid water particles that traveled into the camera fields of view.

Figure 40 illustrates the parts of the spacecraft directly illuminated by the Sun when the spacecraft attitude changes from Sun-point to attitudes for observing. Portions of the OSIRIS-REx spacecraft nadir deck receiving direct solar illumination are colored green for: 71.1°, 64.6° and 54.3° angles of incidence. These illumination geometries match those from the April 10 and 11, 2017 observations when anomalous object activity was particularly high. A comparison of the illumination geometries with the object activity indicates the activity correlates with fresh illumination of the areas circled in black. As sunlight begins illuminating portions of the deck toward the high-gain antenna that are typically shaded, we believe those regions release water-ice particles into the camera fields of view. The lower area is probably where most of the objects originate due to the directional analysis of the ob-

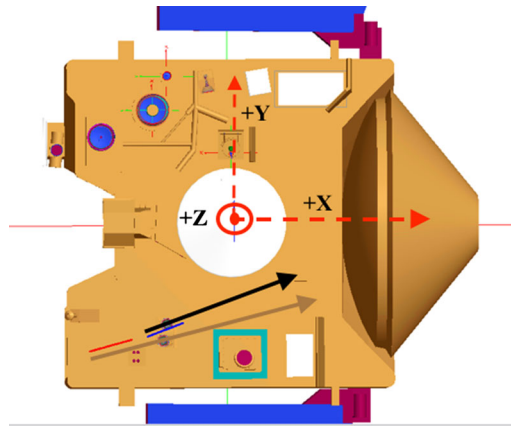


**Fig. 39** Diagram of the spacecraft nadir deck from the OSIRIS-REx non-sequential ray trace model. The XYZ spacecraft coordinate system and origin location are shown as an overlay. The SRC is the white circle in the center of the figure. The high-gain antenna dominates the right side of the figure. The blue line on the deck represents a theoretical line constrained to the plane defined by the vectors from reverse ray tracing a series of points with a  $90^\circ$  orientation (Fig. 37) from the center of the field of view of the NavCam 1 detector plane. The red line represents a theoretical line constrained to the plane defined by the vectors from reverse ray tracing a series of points with a  $90^\circ$  orientation (Fig. 37) from the center of the field of view of the NavCam 2 detector plane. The black arrow shows the location of the suspected origin from which the bulk of the NavCam 1 anomalous objects originate. The brown arrow shows the location of the suspected origin from which the bulk of the NavCam 2 anomalous objects originate

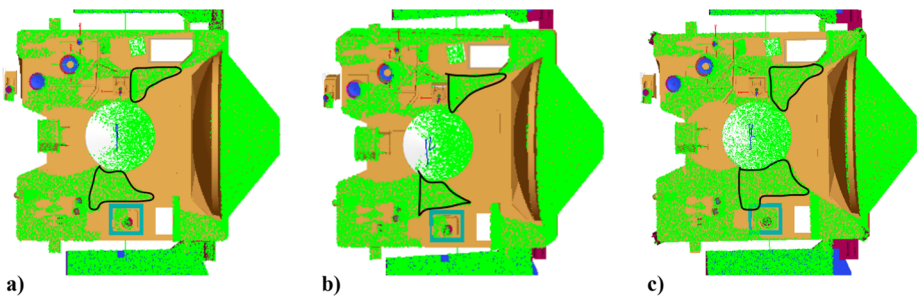


**Fig. 40** Portions of the OSIRIS-REx spacecraft nadir deck receiving direct solar illumination shown in green for  $71.1^\circ$  (a)  $64.6^\circ$  (b) and  $54.3^\circ$  (c) angles of incidence. These illumination geometries match those from April 10 and 11, 2017, when anomalous object activity was particularly high. A comparison of the illumination geometries with the object activity indicates that the activity is correlated with fresh illumination of the areas circled in black. As sunlight begins illuminating portions of the deck toward the high-gain antenna that are typically shaded, we believe these regions release water-ice particles into the camera fields of view. The lower area is likely where most of the objects originate due to the directional analysis of the object streaks and the proximity of the area to the NavCam 1 and 2 locations (near the bottom left corner of the figure). The SRC and distance from the upper area likely preclude either NavCam 1 or NavCam 2 from seeing many particles from that area, but an origin in that vicinity would correlate with the high (near  $180^\circ$ ) and low orientation angles (near  $0^\circ$ ) in the data (Fig. 38)

ject streaks and the proximity of the area to the NavCam 1 and NavCam 2 location (near the bottom left corner of the figure). The SRC and distance from the upper area likely preclude either NavCam 1 or NavCam 2 from seeing many particles from that area but an origin in

that vicinity is consistent with the high (near  $180^\circ$ ) and low orientation angles (near  $0^\circ$ ) in the data.

Subsequent analysis of similar anomalies in OCAMS (OSIRIS-REx Camera System) MapCam (Rizk et al. 2018) images from March and April of 2017 by Rizk et al. (2019) provided additional insight into the activity. MapCam's constrained depth-of-field allowed the calculation of velocity for some objects, finding an average speed of 1 m/s. Object diameter estimates were on the order of  $100 (\pm 60) \mu\text{m}$ . The point of origin for most of the MapCam objects was located near the upper right part of the upper source region highlighted in Fig. 40c.

Some of the anomalous objects that NavCam 1, NavCam 2 and MapCam observed (Rizk et al. 2019), did not follow perfectly linear trajectories – indicating that a force is causing in-flight acceleration. The brightest streak in Fig. 37 is one example of this. The leading explanations for this are asymmetric sublimation of the objects or motion caused by the heliospheric magnetic field and triboelectric charging of the objects. Tenuous features emanating off the side of the anomalies that one could interpret as jets are recorded in the NavCam data, but due to the unresolved nature of the observation it is difficult to conclude with any certainty whether sublimation is being observed.

Because of the anomaly observations and the continued observation of trajectory changes due to suspected outgassing activity, the OSIRIS-REx project pursued a dedicated outgassing campaign to drive the majority of the remaining water out of the SRC and eliminate water-ice contamination from cold-traps on the spacecraft deck (Sandford et al. 2020). This was done by rotating the spacecraft deck generally toward the sun to directly shine sunlight on the SRC and the cold-traps while avoiding the solar keep-out zones of the instruments that could be damaged from direct solar illumination. This activity was completed in between the Launch +6 Month and +18 Month calibration campaigns (primarily during the latter part of 2017) and produced a calibration dataset with considerably fewer anomalies. It appears that the outgassing activity succeeded in eliminating the bulk of the source of the anomalous objects, which will benefit the camera observations of Bennu.

## 9.5 Summary and Conclusions

The TAGCAMS in-flight calibration dataset provides the relevant information to enable the three cameras – NavCam 1, NavCam 2 and StowCam – to complete their primary observation goals during asteroid operations: navigation, sample acquisition, sample stowage and supplementary imaging for OSIRIS-REx science investigations. We assessed the key performance parameters including: linearity, responsivity (both point-source and extended body), dark current, hot pixels, pointing, image geometry transformation, image quality, and stray light (both in-field and out-of-field) from in-flight data collected during the spacecraft's outbound cruise and either confirmed the continued validity of the ground test results or substantially improved upon them.

The most important TAGCAMS performance parameters are arguably the NavCam 1 and 2 pointing knowledge and image geometry transformations due to their role in asteroid proximity maneuvers and sample acquisition. We fully characterized these parameters over the temperature range expected during asteroid operations. We acquired these data by establishing operations-like temperature gradients using operations-like solar illumination geometries and two independent teams reduced the data using different camera models. We have confidence that the TAGCAMS will fulfill its key roles for OSIRIS-REx.

OSIRIS-REx acquired the first TAGCAMS images in support of Bennu operations in October 2018 and has been acquiring TAGCAMS images every day following. In preparation



for this, we used the in-flight calibration to select exposure times and camera settings to optimize the information return in support of navigation and science observations. We expect that as we use TAGCAMS more and learn new information about Bennu and its environment, we will continue to mine information from this comprehensive calibration dataset. Although we may complete spot checks of certain parameters in advance of critical operations, the present calibration will remain in use throughout asteroid operations.

**Acknowledgements** We acknowledge the tremendous efforts of the entire OSIRIS-REx team, past and present, that supported us in the planning, acquisition and return to Earth of the TAGCAMS in-flight calibration dataset. It has proven to be extremely useful in planning our TAGCAMS asteroid operations. This material is based upon work supported by NASA under Contracts NNM10AA11C, NNG12FD66C and NNG13FC02C issued through the New Frontiers Program.

**Publisher's Note** Springer Nature remains neutral with regard to jurisdictional claims in published maps and institutional affiliations.

## References

- B.E. Bayer, Color Imaging Array, United States Patent #3,971,065, Eastman Kodak Company (July 20, 1976)
- B.J. Bos, Design, Calibration and Operation of Mars Lander Cameras. Ph.D. dissertation, University of Arizona (2002). <http://hdl.handle.net/10150/289838>
- B.J. Bos et al., Touch And Go Camera System (TAGCAMS) for the OSIRIS-REx Asteroid Sample Return mission. *Space Sci. Rev.* **214**, 37 (2018). <https://doi.org/10.1007/s11214-017-0465-2>
- B. Bos, C. Jackman, D.S. Lauretta, Origins, spectral interpretation, resource identification, security, regolith explorer (OSIRIS-REx): Touch-And-Go Camera Suite (TAGCAMS) bundle, urn:nasa:pds:orex.tagcams, NASA Planetary Data System (2019)
- D. Brown, Decentering distortion of lenses. *Photogramm. Eng.* **32**(3), 444–462 (1966)
- G.N. Chander et al., Applications of spectral band adjustment factors (SBAF) for cross-calibration. *IEEE Trans. Geosci. Remote Sens.* **51**, 1267–1281 (2013)
- J.A. Christian, L. Benhacine, J. Hikes, Geometric calibration of the Orion optical navigation camera using star field images. *Adv. Astronaut. Sci.* **157**, 769–780 (2016)
- P.B. Davenport, A vector approach to the algebra of rotations with applications. NASA TN D-4696 (1968)
- D.R. Doelling et al., The radiometric stability and scaling of collection 6 Terra- and Aqua-MODIS VIS, NIR, and SWIR spectral bands. *IEEE Trans. Geosci. Remote Sens.* **53**, 4520–4535 (2015)
- D.R. Doelling, C.O. Haney, B.R. Scarino, A. Gopalan, R. Bhatt, Improvements to the geostationary visible imager ray-matching calibration algorithm for CERES Edition 4. *J. Atmos. Ocean. Technol.* **33**, 2679–2698 (2016)
- D. Doelling, C. Haney, R. Bhatt, B. Scarino, A. Gopalan, Geostationary visible imager calibration for the CERES SYN1deg edition 4 product. *Remote Sens.* **10**, 288 (2018). <https://doi.org/10.3390/rs10020288>
- D. Doelling et al., Inter-calibration of the OSIRIS-Rex NavCam with Earth viewing imagers. *Remote Sens.* **11**(22), 2717 (2019). <https://doi.org/10.3390/rs11222717>. 22
- D.S. Lauretta et al., OSIRIS-REx: sample return from asteroid (101955) Bennu. *Space Sci. Rev.* **212**, 925 (2017). <https://doi.org/10.1007/s11214-017-0405-1>
- W.P. Menzel, J.F. Purdom, Introducing GOES-I: the first of a new generation of geostationary operational environmental satellites. *Bull. Am. Meteorol. Soc.* **75**, 757–782 (1994). [https://doi.org/10.1175/1520-0477\(1994\)075<0757:IGITFO>2.0.CO;2](https://doi.org/10.1175/1520-0477(1994)075<0757:IGITFO>2.0.CO;2)
- Z. Milenkovich, C. D'Souza, The Space Operations Simulation Center (SOSC) and closed-loop hardware testing for Orion rendezvous system design, in *AIAA Guidance, Navigation, and Control Conference* (2012), pp. 1–16, 13–16
- OpenCV Dev Team, *Camera Calibration and 3D Reconstruction* (2014)
- J. Pankove, *Optical Processes in Semiconductors* (Dover, New York, 1971)
- B. Rizk et al., OCAMS: the OSIRIS-REx camera suite. *Space Sci. Rev.* **214**, 26 (2018). <https://doi.org/10.1007/s11214-017-0460-7>
- B. Rizk et al., OSIRIS-REx low-velocity particles during outbound cruise. *Adv. Space Res.* **63**, 672–691 (2019). <https://doi.org/10.1016/j.asr.2018.08.020>
- S.A. Sandford et al., Outgassing from the OSIRIS-REx sample return capsule: characterization and mitigation. *Acta Astronaut.* **166**, 391–399 (2020). <https://doi.org/10.1016/j.actaastro.2019.07.043>

- B.R. Scarino et al., A web-based tool for calculating spectral band difference adjustment factors derived from SCIAMACHY hyperspectral data. *IEEE Trans. Geosci. Remote Sens.* **54**, 2529–2542 (2016). <https://doi.org/10.1109/TGRS.2015.2502904>
- G. Wahba, A least squares estimate of satellite attitude. *Problem 65-1. SIAM Rev.* **7**(3), 409 (1965)
- C. Wright, A. Liounis, B. Ashman, Optical navigation algorithm performance, in *1st Annual RPI Workshop on Image-Based Modeling and Navigation for Space Applications* (2018)
- X. Xiong, *MODIS Reflective Solar Calibration and Uncertainty Assessment* (2011). [http://gsics.atmos.umd.edu/pub/Development/20110322/Day2pm\\_GRWG\\_Xiong\\_MODIS.pdf](http://gsics.atmos.umd.edu/pub/Development/20110322/Day2pm_GRWG_Xiong_MODIS.pdf) (Accessed 7 November 2017)
- X. Xiong, W.L. Barnes, An overview of MODIS radiometric calibration and characterization. *Adv. Atmos. Sci.* **23**, 69–79 (2006). <https://doi.org/10.1007/s00376-006-0008-3>